Precision measurement of the 1S ground-state Lamb shift in atomic hydrogen and deuterium by frequency comparison

M. Weitz, A. Huber, F. Schmidt-Kaler,* D. Leibfried, W. Vassen,† C. Zimmermann, K. Pachucki, and T. W. Hänsch
Max-Planck-Institut für Quantenoptik, 85748 Garching, Germany

L. Julien and F. Biraben
Laboratoire Kastler Brossel, Université Pierre et Marie Curie, 75230 Paris Cedex 05, France
(Received 2 May 1995)

We have measured the hydrogen and deuterium $1S$ Lamb shift by direct optical frequency comparison of the $1S$-$2S$ and $2S$-$4S/4D$ two-photon transitions. Our result of 8172.874(60) MHz for the $1S$ Lamb shift in hydrogen is in agreement with the theoretical value of 8172.802(40) MHz. For the $1S$ Lamb shift in deuterium, we obtain a value of 8183.807(78) MHz, from which we derive a deuteron matter radium of 1.945(28) fm. The precision of our value for the $1S$ Lamb shift has surpassed that of radio frequency measurements of the $2S$-$2P$ Lamb shift. By comparison with a recent absolute measurement of the hydrogen $1S$-$2S$ transition frequency, we deduce a value for the Rydberg constant $R_\infty = 109\,737.315\,684\,9(30)\ \mathrm{cm}^{-1}$.

PACS number(s): 32.30.Jc, 06.20.Jr

I. INTRODUCTION

The hydrogen atom plays a unique role in atomic physics. Because of its simple configuration (one proton and one electron) it can be described with an unequalled level of precision, which allows stringent tests of fundamental physics laws and the determination of fundamental constants [1]. Measurements of the hydrogen $2S$ Lamb shift by rf spectroscopy have long provided one of the best tests of quantum electrodynamic theory (QED) [2,3]. Further improvements appear now limited by the 100-MHz natural linewidth of the nearby $2P$ state.

In this paper, we report of a measurement of the $1S$ ground state Lamb shift that does not suffer from this limitation. We determine the $1S$ Lamb shift by measuring the difference between the frequency of the $2S$-$4S$ (respectively $2S$-$4D$) transition and a quarter of the $1S$-$2S$ transition frequency. In this difference the main energy contributions, described by the simple Rydberg formula $E_n = -R/n^2$, cancel out. From the relatively small residual frequency difference of about 5 GHz the $1S$ Lamb shift can be derived [4]. Since most quantum electrodynamic effects scale with the principle quantum number n as $1/n^3$, the $1S$ Lamb shift is the largest in atomic hydrogen. The $1S$-$2S$ two-photon transition has a natural linewidth of only 1.3 Hz, and experimentally [5] has recently been resolved to 1 part in 10^{11}. The natural linewidths of the $2S$-$4S$ and $2S$-$4D$ two-photon transitions, 0.704 and 4.36 MHz, are well below that of the $2S$-$2P$ transition.

By comparison of the sharp two-photon transitions, we have determined the $1S$ Lamb shift to 7.5 parts in 10^6 for hydrogen and 1 part in 10^5 for deuterium. Our measurements may be considered as the best test of quantum electrodynamics on a bound atomic system to date. Compared to the previous generation measurements of the $1S$ Lamb shift [6,7] an order of magnitude increase in accuracy has been achieved. Very recently, one of us (K.P.) has obtained an unexpectedly large value for two-loop binding corrections to the Lamb shift [8,9]. These contributions shift the theoretical value of the hydrogen $1S$ Lamb shift down by 295 kHz and bring experiment and theory, based on a proton charge radius as measured by Simon *et al.* [10], into agreement. Previously a disagreement of up to three standard deviations remained between experiment and theory for both the $1S$ (Refs. [11,12], and Refs. [13,14] combined) and $2S$ (Refs. [2,3]) Lamb shifts. While the new theoretical results bring theory and experiment into agreement for hydrogen, a measurement of the $2S$-$2P$ splitting of the He^+ ion based on observation of the quench radiation asymmetry in a static electric field [15] does not agree with theory any more.

In two recent Letters [11,12] we have described measurements of the $1S$ Lamb shift in hydrogen and deuterium. We give here a detailed description of the experimental setup and the data analysis. Since a detailed description of the $1S$-$2S$ spectrometer has been published elsewhere [5], we concentrate here on the $2S$-$4S$ spectrometer. Due to the larger natural linewidths of $2S$-$4S$,$4D$, this spectrometer limits our experimental accuracy. For our data analysis, we use the latest values for the excited state Lamb shifts and fundamental constants. Therefore our results differ slightly from earlier published values [12].

The quantum electrodynamic contributions to the Lamb shift are quite similar for hydrogen and deuterium. From the measured difference of the hydrogen and deuterium Lamb shifts [or from the isotope shift of $(E_{4S}-E_{2S})-\frac{1}{4}(E_{2S}-E_{1S})$] we can determine the rms difference of deuteron and proton nuclear charge radii, from which we derive the deuteron matter radius. We note that in a direct measurement of the hydrogen deuterium isotope shift of the $1S$-$2S$ transition [16] a more accurate result for the deuteron matter radius was obtained due to the high Q of the $1S$-$2S$ transition. Using both

*Present address: Ecole Normale Superieure, 75231 Paris Cedex 05, France.

†Present address: Vrije Universiteit, Faculteit Natuurkunde en Sterrenkunde, 1081 HV Amsterdam, Netherlands.

measurements, terms scaling as $1/n^2$ and $1/n^3$ can be eliminated and simultaneous determination of the electron to proton mass ratio and nuclear size or structure effects is possible.

II. ENERGY LEVELS OF THE HYDROGEN ATOM

Neglecting hyperfine structure, the hydrogen energy levels are given by the sum of the following contributions [17]:

$$E(n,J,L)=E_{\rm DC}(n,J)+E_{\rm RM}(n,J)+E_{\rm LS}(n,J,L), \quad (1)$$

where $E_{\rm DC}$ denotes the Dirac-Coulomb energy as the main energy contribution, $E_{\rm RM}$ the leading recoil corrections due to the finite mass of the nucleus, and $E_{\rm LS}$ the Lamb shift. Since the first two energy contributions are well-known functions of the Rydberg constant R_∞, the fine structure constant α and the ratio of the electron and nuclear mass m_e/m_N, we briefly discuss here the last contribution.

The Lamb shift contains QED corrections and corrections for the finite size and polarizability of the nucleus. Reviews of the contributions in hydrogenic atoms have been given by Erickson [18], Johnson and Soff [17], Sapirstein and Yennie [19], and will be given by Pachucki *et al.* [9]. We follow here mainly the latter reference; for some corrections to the $4D$ energy not included in Ref. [9] we use results given by Erickson [18]. The Lamb shift can be written as

$$E_{\rm LS}(n,J,L)=\frac{\alpha(Z\alpha)^4 m_e c^2}{n^3 \pi h} F(Z\alpha), \quad (2)$$

$$F(Z\alpha)=F_\infty(Z\alpha)+F_{\rm RR}(Z\alpha)+F_{\rm NR}(Z\alpha)+F_{\rm NS}+F_{\rm Pol}, \quad (3)$$

where $\alpha(Z\alpha)^4 m_e c^2/\pi h=2(Z\alpha)^4 cR_\infty/\pi\alpha$ =813.862 88(11) MHz for $Z=1$. For an infinitely heavy point nucleus, $F(Z\alpha)$ can be expanded as

$$F_\infty(Z\alpha)=A_{40}+\ln(Z\alpha)^{-2}A_{41}+(Z\alpha)A_{50}+(Z\alpha)^2\{A_{60}+\ln(Z\alpha)^{-2}A_{61}+\ln^2(Z\alpha)^{-2}A_{62}\}+\cdots+\frac{\alpha}{\pi}(B_{40}+\alpha B_{50})+\cdots. \quad (4)$$

The dimensionless coefficients A_{pq} and B_{pq} depend on the quantum numbers L and J, some of them also on n. Terms with A_{pq} correspond to self-energy and vacuum polarization (one-loop corrections); terms with B_{pq} give corrections due to two-loop diagrams. The calculation of two-loop binding corrections B_{50} has been completed very recently by one of us [8]. A surprisingly large $B_{50}=-21.4(1)$ for S states was obtained, contributing -295 kHz to the $1S$ Lamb shift [8,9].

If we account for nuclear recoil motion due to the finite nuclear mass, further corrections occur. These contributions are usually divided into the radiative and nonradiative recoil corrections $F_{\rm RR}$ and $F_{\rm NR}$, which are now known with sufficient precision [20,9]. The finite nuclear size also causes an energy shift for S states. This contribution can be calculated in nonrelativistic perturbation theory:

$$F_{\rm NS}=\left(\frac{\mu}{m_e}\right)^3\frac{2\pi\alpha}{3}\left(\frac{r_{\rm ch}}{r_e}\right)^2\delta_{L0}, \quad (5)$$

TABLE I. Theoretical Lamb shifts as discussed in Sec. II.

State	Hydrogen (MHz)	Deuterium (MHz)
$1S_{1/2}$	8172.802(40)	8183.785(47)
$2S_{1/2}$	1045.003(5)	1046.375(6)
$2P_{1/2}$	−12.8357(15)	−12.8349(15)
$4S_{1/2}$	131.6752(6)	131.8468(7)
$4D_{3/2}$	−0.5204(1)	−0.5205(1)
$4D_{5/2}$	0.5364(1)	0.5370(1)

where $r_{\rm ch}$ denotes the rms nuclear charge radius, $r_e=\alpha^2 a_0$ the classical electron radius, and μ the reduced mass [19]. Corrections due to the nuclear polarizability are accounted for in $F_{\rm Pol}$, which contribute about -60 Hz/n^3 and $-22(2)$ kHz/n^3 for hydrogen and deuterium, respectively [21,22].

The rms charge radius of the deuteron $r_{{\rm ch},d}$ can be calculated [2,3] from the rms charge radius of the proton $r_{{\rm ch},p}$ and the deuteron matter radius $r_{E,d}$:

$$r_{{\rm ch},d}^2=r_{{\rm ch},p}^2+r_{E,d}^2+r_n^2+\frac{3\hbar^2}{4m_p^2c^2}, \quad (6)$$

where $r_n^2=-0.1192(18)$ fm^2 denotes the neutron charge radius and $3\hbar^2/4m_p^2c^2=0.033\,17$ fm^2 is the Zitterbewegung contribution. For a calculation of the theoretical Lamb shifts, we use a proton charge radius $r_{{\rm ch},p}=0.862(12)$ fm measured by Simon *et al.* [10] and a deuteron matter radius $r_{E,d}=1.953(3)$ fm derived in an analysis by Klarsfeld *et al.* [23] (which however is probably too low, see Sec. V C). This results in a deuteron charge radius $r_{{\rm ch},d}=2.115(6)$ fm. Our results for the theoretical Lamb shifts of the states $1S$, $2S$, $2P_{1/2}$, $4S$, and $4D$ are presented in Table I. The different contributions to the $1S$ Lamb shift are given in Table II for hydrogen and deuterium. The differences of these values compared to those quoted in our previous paper [12] are due to the new result for B_{50}, and some more precise values for higher order self-energy, radiative, and nonradiative recoil corrections [20,9]. For deuterium we now also include small corrections due to the nuclear polarizability [22] and a spin-dependent recoil contribution [24]. We use the 1986 recommended fundamental constants [25], except for recent, more accurate determinations of the Rydberg constant [14]

TABLE II. Contributions to the $1S$ Lamb shift of hydrogen and deuterium as discussed in Sec. II.

Energy contributions	Hydrogen (MHz)	Deuterium (MHz)
Self-energy	8396.456(1)	8396.456(1)
Vacuum polarization	−215.168(1)	−215.168(1)
QED higher order	0.724(24)	0.724(24)
Radiative recoil corr.	−12.778(6)	−6.396(3)
Nonradiative recoil corr.	2.402(1)	1.190(1)
Nuclear size	1.167(32)	7.002(40)
Nuclear polarizability	0.000(0)	−0.022(2)
Sum	8172.802(40)	8183.785(47)

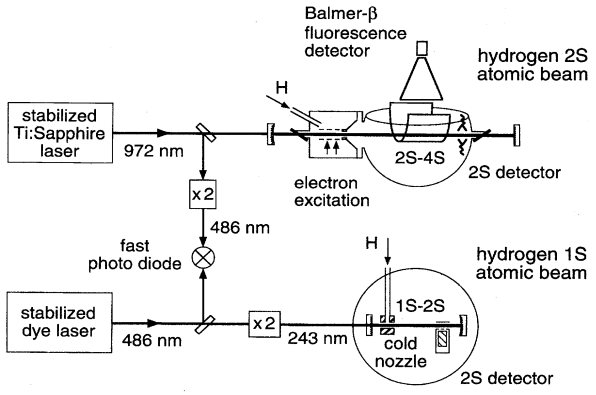

FIG. 1. Experimental setup for measurement of the $1S$ Lamb shift in atomic hydrogen and deuterium.

$R_\infty = 109\,737.315\,683\,4(24)\ \mathrm{cm}^{-1}$, the electron proton mass ratio [26] $m_e/m_p = 1/1836.152\,664\,6(58)$, and the deuteron proton mass ratio [27] $m_d/m_p = 1.999\,007\,501\,3(14)$. The influence of these newer values on our results for the experimental $1S$ Lamb shift is negligible. Our result for the Rydberg constant is slightly affected by using the more recent value for m_e/m_p.

III. EXPERIMENTAL SETUP

Our experimental setup for measurement of the $1S$ Lamb shift by comparison of the $1S$-$2S$ and $2S$-$4S$,$4D$ two-photon transitions is shown in Fig. 1. For the $1S$-$2S$ spectrometer a very frequency stable blue dye laser is doubled to produce ultraviolet light near 243 nm. The $1S$-$2S$ transition is excited by Doppler-free two-photon spectroscopy of a cold hydrogen atomic beam with a collinear standing wave of the ultraviolet light. A Ti:sapphire laser produces light near 972 nm to excite the Doppler-free $2S$-$4S$ and $2S$-$4D$ two-photon transitions in a beam of metastable hydrogen atoms, which have been excited into the metastable level by electron impact. The $1S$ Lamb shift is obtained by measuring the small frequency difference between the doubled infrared light and part of the blue dye laser light as a beat node on a fast photodiode.

A. The $1S$-$2S$ spectrometer

The $1S$-$2S$ spectrometer has been described elsewhere in detail [5,28]. We use a commercial cw dye laser (Coherent 699-21) emitting about 500 mW light near 486 nm, which is pumped by a 6-W krypton-ion laser. The dye laser frequency is locked to an external reference cavity using a radio-frequency sideband technique [29]. Inside the laser cavity a galvo-mounted Brewster plate, a piezo-mounted mirror, and an additional electro-optical modulator compensate for frequency fluctuations with a servo bandwidth of about 1.5 MHz. The reference cavity consists of a Zerodur spacer with gyroscope quality mirrors contacted to the ends. The spacer is suspended by soft springs in vacuum chamber in order to minimize the transport of acoustic noise to the resonator. Whereas the laser frequency is locked to the resonator to within a rms linewidth of 10 Hz, the absolute frequency stability of the laser is limited by the stability of the reference cavity to a linewidth of about 1.5 kHz. The laser frequency can be tuned by changing the drive frequency of an acousto-optic modulator which is placed between laser and reference cavity. The blue light of the dye laser is coupled into a ring buildup cavity, where a β-barium borate crystal generates about 15 mW of second harmonic light at 243 nm. This UV light is coupled into a linear enhancement cavity inside an atomic beam apparatus, producing a standing wave field of up to 90 mW power.

Molecular hydrogen is dissociated in a microwave discharge. A nozzle, which can be cooled to the temperature of liquid nitrogen or helium, emits an atomic beam collinear to the optical standing wave. Hydrogen atoms in the $1S$ ground state are excited by Doppler-free two-photon transitions into

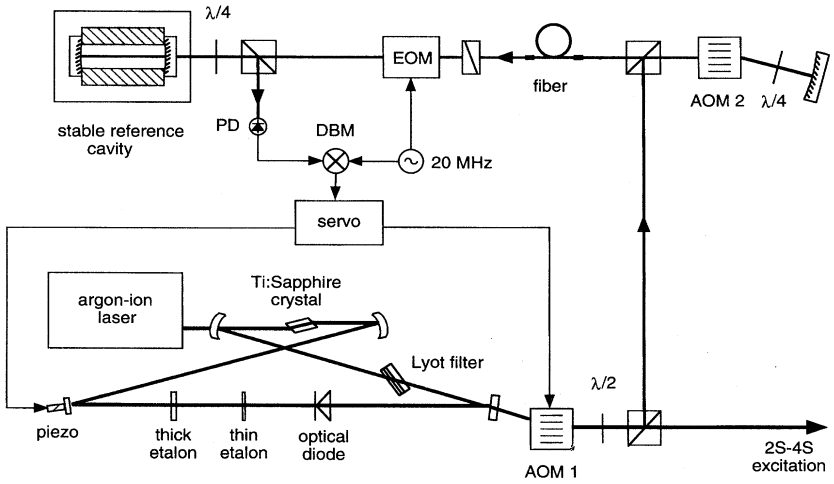

FIG. 2. Ti:sapphire laser with frequency stabilization (EOM: electrooptic modulator; AOM: acoustooptic modulator; PD: photodiode; DBM: doubly balanced mixer).

the metastable $2S$ state. After an 11-cm-long interaction region the atoms enter the detector, where a small electric field mixes the $2S$ and $2P$ states. The excited atoms decay and emit a Lyman-α photon, which can be detected with a solar-blind photomultiplier. If the nozzle is cooled to the temperature of liquid nitrogen, the observed linewidth is about 30 kHz at 243 nm for hydrogen.

For measurement of the $1S$ Lamb shift, the laser frequency is locked to the maximum of the $1S$-$2S$ signal with a personal computer (see Sec. IV A).

B. The 2S-4S spectrometer

1. Stabilized Ti:sapphire laser

The light at 972 nm for two-photon excitation of the $2S$-$4S$ and $2S$-$4D$ transitions is produced by a Ti:sapphire laser (Fig. 2). We use a commercial cw ring laser (Schwartz Electro-Optics) that is frequency locked to an external stable reference cavity [30,31].

The Ti:sapphire laser is pumped by 10 W at 488/514 nm from an argon-ion laser (all lines), and produces about 1 W infrared light near 972 nm. The high pump power level and the long wavelength requires a special optical diode consisting of a strongly rotating terbium gallium garnet crystal Faraday rotator and an optically active plate. In contrast to the commercial version, we have replaced the 1-mm uncoated etalon by two uncoated 0.2- and 3-mm étalons, which improves the stability at high pump powers.

The linewidth of the free running laser is of the order of several MHz. We have stabilized the frequency of the laser to a longitudinal mode of a stable reference cavity consisting of two mirrors of high reflectivity (finesse=2000), which are contacted to the same Zerodur spacer as used for the blue dye laser reference cavity. The Ti:sapphire laser is tuned by varying the drive frequency of an acousto-optic modulator (AOM 2) placed between the laser and reference cavity. In order to correct for the frequency-dependent deviation angle, the modulator is used in double pass. An error signal— representing the frequency difference between laser and reference cavity—is generated with a radio frequency sideband technique [29]. The error signal is amplified and integrated. Frequency components of the error signal up to about 5 kHz are fed to a piezo-mounted mirror in the laser, whereas frequency components between 5 and 150 kHz are fed to a voltage controlled oscillator, which drives an acousto-optic modulator (AOM 1) right behind the laser. The faster branch of the servo loop appeared to be important especially when higher argon-ion laser pump powers (about 10 W) were used. At higher pump powers the amplitude noise of the argon-ion laser increases strongly, leading to fluctuations in the Ti:sapphire laser crystal temperature, which are converted into frequency noise due to the temperature-dependent refractive index of the crystal [32].

At 1 W output power the laser rms linewidth relative to the cavity is about 700 Hz. The actual linewidth of the laser has been determined by measuring the beat signal between the frequency doubled Ti:sapphire laser light with the highly stable dye laser to be less than 10 kHz.

2. Atomic beam apparatus for metastable 2S atoms

The atomic beam apparatus of the $2S$-$4S$,$4D$ spectrometer is shown in Figs. 1 and 3. We produce a metastable hydrogen beam in two steps [33]. Molecular hydrogen flows through a needle valve into a Pyrex glass tube (inner diameter 10 mm) that narrows at the end to an inner diameter of 2 mm. The tube is placed inside an air-cooled microwave resonator driven by 20 W microwave power at 2.45 GHz. At an optimum hydrogen pressure of about 0.6 mbar a red discharge can be excited. With this kind of discharge a dissociation degree of 90% has been reported [34].

The hydrogen is guided by Teflon tubes into a first vacuum chamber. This chamber is evacuated with a turbo pump (Leybold Turbovac 360 V, pumping speed for H_2: 330 l/s) to a pressure of about 1×10^{-4} mbar with hydrogen flow. We estimate an atomic hydrogen flux of 1×10^{18} per second. In order to avoid oil degradation inside the turbo pump due to atomic hydrogen, the turbo pump bearings were flushed with nitrogen gas. The ratio of nitrogen to hydrogen flow is about 6 to 1. In this first vacuum chamber, the hydrogen atoms are excited into the metastable $2S$ state by electron impact. Electrons are emitted by three closely spaced thorium doped tungsten filaments (0.25-mm diameter) and accelerated by an average voltage of 12.8 V. The cathode current reaches a value of 6 mA at a heating current of 15.8 A. Hydrogen atoms are emitted from a 3-mm-diam Teflon nozzle. Since the metastable $2S$ atoms are quenched easily by electric fields due to the nearby $2P$ state, the excitation and transport of the metastable atoms takes place in a Faraday cage. The electron momentum transfer deflects the hydrogen atoms onto the laser axis. The angle between the initial hydrogen beam and the laser axis is 20°; the divergence angle of the metastable hydrogen beam produced is about 10° [33]. The position of the nozzle is adjusted for optimum efficiency of metastable atom production.

For two first sets of measurements we used an early version of the electron gun with a single tungsten filament. The new electron gun with the thorium doped tungsten filaments was designed mainly to minimize the emitted light and thus the background for the Balmer-β fluorescence signal, but also provided a four times higher metastable flux than previously. This is mainly due to the lower work function of thorium doped tungsten.

The excited atoms leave the first vacuum chamber through an aperture of 4-mm diameter and enter a second

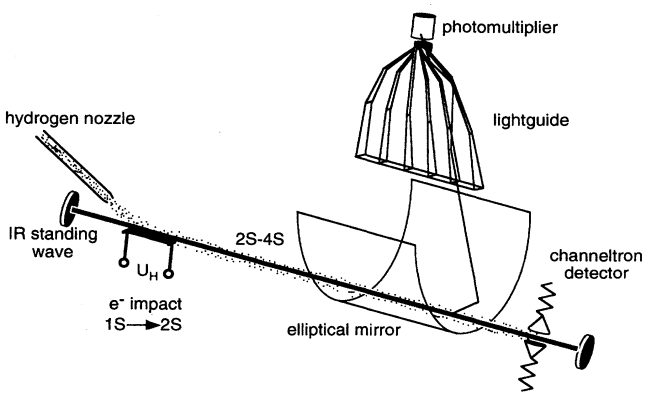

FIG. 3. Metastable hydrogen atomic beam apparatus with fluorescence detector.

vacuum chamber, where they travel collinearly with the laser beam along a 33-cm-long interaction region, until they are detected behind a second aperture of 2.5-mm diameter. The second vacuum chamber is evacuated by a turbo pump identical to the one used for the first chamber. Because of the lower gas load, the pressure here is about 6×10^{-6} mbar. Differential pumping is necessary to ensure a high flux of hydrogen atoms as well as a low background pressure.

The metastable atoms are detected after the second aperture with a channeltron detector as shown in Fig. 4. An electric field of about 50 V/cm is generated by two wires, which are oppositely charged (± 12 V) in order to appear neutral in the far field. This quench field mixes the $2S$ and $2P$ states; the metastable atoms decay and emit a Lyman-α photon, which can be detected by two potassium-iodate coated channeltrons (CEM 4039, Galileo). The quantum efficiency of the coated channeltrons is 20–40 % [35]. The cones of the channeltrons are negatively charged (-70 V) to minimize background pulses from electrons emitted by the filament. The total quantum efficiency of this detector was measured to be better than 10%. During the experiment, the metastable count rate is detected during a period of 0.5 s with applied quench voltage, followed by a second period of 0.5 s without quench voltage. Subtracting the two count rates eliminates a small quench field-independent background, which is caused mainly by Lyman-α photons emitted from the electron impact excitation region. With the latest version of the electron gun we observe typical metastable count rates of 100 000 per second. Using the heavier and thus slower deuterium atoms, the count rate is about 40% higher.

For our latest measurements the $2S$-$4S$ transition was detected not only by monitoring the metastable flux, but also by simultaneously observing the blue $4S$-$2P$ Balmer-β fluorescence along a 15-cm-long part of the atomic beam starting 15 cm behind the first aperture. The $4S$-$2P$ decay channel has a branching ratio of 58% [36]. One crucial experimental problem was to guide the divergent fluorescence radiation to a photomultiplier tube with high quantum efficiency. Principles of nonimaging optics have been reviewed by Welford and Winston [37]. We used an elliptical mirror (aluminum galvanically coated with silver) which images the atomic beam through a vacuum window onto a focal line outside the vacuum apparatus, as shown in Fig. 3. Endcaps (not shown in Fig. 3) let the mirror appear infinitely long. A Plexiglas lightguide with its entrance facet along the outside focal line of the elliptical mirror guides the fluorescence light via multiple internal total reflections onto the 21-mm-diam entrance window of the photomultiplier (Hamamatsu R1924, quantum efficiency at 486 nm: 18%). The lightguide is subdivided into five segments which overlap in the photomultiplier, but do not touch each other. Subdividing the lightguide into segments increases its efficiency, since in this way only a slight focusing of the light in the direction longitudinal to the atomic beam is necessary, and thus the longitudinal acceptance angle for total internal reflection is increased. A numerical Monte-Carlo simulation was used to calculate a quantum efficiency of 25% for the mirror and 65% for the lightguide. It also allowed the iterative optimization of the system.

For reduction of stray light from the filament a combination of Schott color filters with a transmission bandwidth of 90 nm FWHM around 486 nm was placed below the entrance facet of the lightguide. Most of the 1800-K thermal emission spectrum is shielded from the photomultiplier in this way. Interference filters, although available with spectrally much narrower transmission bandwidth, cannot be used due to their small angular acceptance. The total quantum efficiency of the fluorescence detector for Balmer-β detection is estimated to be about 2%.

For the first and second group of measurements, the interaction region between the two apertures was shielded from electric and magnetic fields using a double Mu-metal tube coated by graphite on the inside. For the more recent measurements with the fluorescence detector this Mu-metal tube could no longer be used. The interaction region is shielded against stray electric fields by a mesh tube coated with colloidal graphite. This grid absorbs only a few percent of the fluorescent light. Since the interaction region is no longer shielded against the earth's magnetic field, we have recorded with the new setup only $2S$-$4S$ lines. These are less sensitive to magnetic fields than the $2S$-$4D$ transitions (see Sec. V A 2).

We have measured the longitudinal velocity distribution of the metastable atomic beam by observing the Doppler-broadened $2S$-$4P$ transition. For this measurement, we have sent about 1 mW of blue light near 486 nm collinear to the metastable beam. In order to avoid the problem of absolute frequency calibration as well as to minimize shifts due to the dynamical Stark effect, a standing wave of blue light was generated with a retroreflecting mirror. During the measurement we have recorded the metastable flux with the channeltron detector while varying the frequency. The frequency axis has been calibrated by two Fabry-Pérot resonators with free spectral ranges of 332 MHz and 7.5 GHz. We observed two minima of the metastable count rate caused by absorption from the copropagating and counterpropagating laser beam. Atoms which are excited into the $4P$ state by the laser field decay (lifetime 12 ns [36]) mainly into the $1S$ ground state. Therefore, when an atomic velocity class is on resonance with the laser, a decrease in metastable flux can be observed. For hydrogen the observed two minima are about 10 GHz apart and have a width of about 5 GHz each. Assuming a velocity distribution of the flux of metastable atoms proportional to $v^4\exp(-v^2/v_0^2)$ [38] for our latest version of the metastable source we obtain $v_0=2580(100)$ m/s for hydrogen and $v_0=1490(100)$ m/s for deuterium. This velocity distribution differs from a Maxwellian atomic flux distribution by an additional factor of v, which is due to the smaller angular dispersion for faster atoms after electron impact ($\rightarrow v^2$) and the fact that the electron excitation probability is proportional to $1/v$.

3. Enhancement resonator

For excitation of the $2S$-$4S$ and $2S$-$4D$ two-photon transitions, we couple about 400 mW of the Ti:sapphire laser radiation into a linear resonator. Optical isolation of the laser is ensured by the acousto-optic modulator (AOM 1 in Fig. 2) which is used also for laser frequency stabilization. The resonator consists of a curved input mirror (radius of curvature -1000 mm, reflectivity 99.4%) and a plane high reflector (reflectivity >99.9%, mounted on a piezo transducer) 710 mm apart. The mirrors are placed outside the vacuum cham-

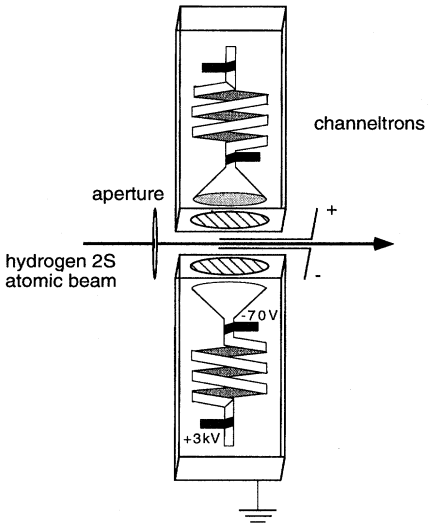

FIG. 4. Channeltron detector for metastable hydrogen atoms.

ber. The light enters the vacuum chamber via two fused silica Brewster windows. The finesse of the resonator is about 500. A servo loop locks the resonator to the Ti:sapphire laser frequency. The error signal for the servo loop is generated by observing the polarization of the reflected light [39] and is amplified, integrated, and fed to the piezo crystal. We obtain a maximum circulating optical power of 40 W on an average beam waist of 0.5 mm.

In an earlier stage of the experiment we observed strong fluctuations of the intracavity power and a breakdown to about 20 W circulating power when the cavity was locked to the laser frequency. At that time we used two thick (9 mm each) quartz Brewster windows. If for testing purposes only one of the windows was left in the resonator, the breakdown occurred at approximately twice the power level. We assume that these observations can be explained by self-focusing of the optical beam due to thermal lensing in the windows. An optical path difference is generated between the beam axis and the $1/e^2$ point which is proportional to the power absorbed in the substrate, but it does not depend on the beam diameter. If the path difference becomes comparable to the optical wavelength, the resonator mode changes significantly and less laser power can be coupled into it. Using the formulas given by Winkler *et al.* [40], we estimate an absorption of the order 1000 ppm/mm for our fused silica quartz windows, which is believed to be caused by OH impurities. Since quartz windows of better purity were not readily available and the breakdown power is inversely proportional to the window thickness, we moved to thinner windows. All results reported below have been obtained using a 1-mm-thick, small Brewster window of a commercial argon-ion laser on the far end side of the resonator and a 5-mm-thick window on the side next to the electron gun. Its larger diameter allows easier removal of filament residues. After these modifications we did not observe any breakdown effects for available power levels.

C. Frequency comparison

About 10% of the Ti:sapphire light is used for frequency doubling in a nonlinear potassium niobate crystal ($KNbO_3$), as shown in Fig. 1. 90° phase matching occurs at a temperature of -19.5 °C. The crystal is placed in a small vacuum chamber (not shown in Fig. 1) to avoid condensation of water. The length of the crystal is 4.6 mm. Using a beam waist of 21 μm in the crystal, we produce about 8 μW of blue light near 486 nm with 100-mW infrared light. The second harmonic is overlapped through a 50:50 beam splitter on a fast photo diode (Antel AR-S2, active area diameter: 60 μm) with about 1 mW of blue light from the $1S$-$2S$ spectrometer. Both beams are carefully mode matched. We observe a beat signal of about 4.8 GHz when comparing the $1S$-$2S$ with the $2S$-$4S$ transition, and 6.5 GHz for the comparison of $1S$-$2S$ with $2S$-$4D_{5/2}$. The signal-to-noise ratio of the beat signal is about 25 dB in 100-kHz bandwidth.

The precise frequency of the beat signal is determined first by a rf spectrum analyzer (HP 79000 A), which is phase locked to a rubidium frequency standard (Rohde & Schwarz, XRKS and XKE 2) which itself is locked to a radio signal of the PTB for compensation of long term drifts (precision $>10^{11}$). The dominating frequency error is caused by the sharp frequency filters in the spectrum analyzer. This error is proportional to the spectrum analyzer bandwidth and was measured to be less than 2 kHz at 486 nm. The frequency of the beat signal is also determined with a frequency counter (Advantest, TR 5214). For proper operation, the counter requires an input signal with the power of the carrier much higher than the integrated noise power in its 500-MHz analysis range. It therefore is necessary to filter the beat signal with a bandwidth of about 1 MHz. Since filters of this low bandwidth are not readily available in the microwave region, the beat signal is mixed down to a radio frequency of about 19 MHz using a microwave synthesizer (also phase locked to the rubidium standard) as a local oscillator, and then filtered by a bandpass. During the measurement, the synthesizer frequency is adjusted for every data point to center the expected counter frequency in the bandpass transmission curve. The obtained signal to noise ratio of 13 dB is sufficient to ensure proper counter operation. For future measurements, the use of a fast avalanche diode or an electronic signal tracker should improve the signal-to-nose ratio.

The $2S$-$4S$,$4D$ spectrometer and data acquisition is controlled with a personal computer that adjusts the frequency of the infrared laser by setting the drive frequency of the acousto-optic modulator (AOM 2). It also controls the microwave local oscillator for the frequency counter. Simultaneously, the computer records the metastable count rate, the fluorescence detector count rate, the beat frequencies as measured by the spectrum analyzer and by the counter, and the power in the enhancement resonator. It also checks the frequency lock of the infrared laser to the stable reference cavity by monitoring the transmitted power. A computer card (Metrabyte, DASH 16) provides the required analog-digital and digital-analog converters and allows counting of the channeltron pulses. The fluorescence photon pulses are counted with a photon counter (Stanford Research).

IV. MEASUREMENTS AND DATA ANALYSIS

In this section we describe the procedure for recording experimental data. The frequency of the blue dye laser is locked to the maximum of the extremely sharp $1S$-$2S$ tran-

sition, which serves as a precise frequency reference for the $2S$-$4S$ spectrometer. The infrared laser is scanned repeatedly over the atomic $2S$-$4S$ and $2S$-$4D$ resonances. Their exact line shapes are recorded and interpreted later. We also describe the calculation of theoretical line shapes for the $2S$-$4S$ and $2S$-$4D$ transitions and how we obtain an accurate comparison of the $1S$-$2S$ with the $2S$-$4S$ and $2S$-$4D$ transition frequencies by fitting the experimental spectra with calculated line shapes.

A. Measurement procedure

For the $1S$-$2S$ transition we have obtained a resolution of 1 part in 10^{11} by cooling the hydrogen atomic beam with a nozzle at the temperature of liquid helium, limited by transit time broadening and by the second order Doppler effect [5]. In our Lamb shift measurements for simplicity we usually operate the beam at liquid nitrogen temperature, resulting in a resolution of 3 parts in 10^{11}. The blue dye laser is locked to the maximum of the $1S$-$2S$ line with a personal computer. The $2S$ signal is recorded first at a frequency about 4 kHz above the atomic resonance, then 4 kHz below the resonance. The difference of the count rates is multiplied with a constant and added to the instantaneous frequency of the laser. We thus obtain a lock to the center of the atomic line with typical fluctuations of a kHz at 486 nm. The frequency error of the $1S$-$2S$ spectrometer is below a kHz, and thus more than an order of magnitude smaller than the statistical and systematic uncertainties associated with the $2S$-$4S$,$4D$ spectrometer.

The infrared laser is scanned continuously over the atomic $2S$-$4S$ and $2S$-$4D$ resonances while the beat frequency with the blue dye laser, locked to $1S$-$2S$, is monitored. Since the electron excitation generates a flux of metastable atoms which fluctuates on a time scale of a few minutes, it is crucial to average many atomic spectra. The spectrum is divided into 100 ($2S$-$4S$) or 200 ($2S$-$4D$) frequency points. For each laser frequency, the metastable count rate is recorded for half a second without and for half a second with applied quench field, while the blue Balmer-β fluorescence is monitored continuously. The infrared laser is then tuned four frequency steps further and the next data point is recorded. The missing frequency points are recorded during the next three spectra. After four frequency sweeps, two with increasing and two with decreasing frequency, all frequency points have been taken once. For every laser power we record 40 ($2S$-$4S$) or 24 ($2S$-$4D$) spectra. One measurement takes about 20 minutes and is repeated for several light powers within a day, in alternating order of laser power.

We have recorded data for the determination of the $1S$ Lamb shift in three measurement periods. Between these periods several changes of the apparatus have been made. The most important change took place between the second and third measurement period, when a detector for observation of the blue $4S$-$2P$ fluorescence has been installed in the $2S$-$4S$ spectrometer. This change resulted in an about twofold reduced statistical error. All previous data had been taken only by observing the decrease in metastable signal. Results of the first measurement period for hydrogen have been published in Ref. [11]. In a second measurement period we have determined both the hydrogen and deuterium $1S$ Lamb shift [31,41]. Since the second measurement period, we have excited the $1S$-$2S$ transition on a hydrogen beam cooled to liquid nitrogen temperature rather than room temperature. Results including the third measurement period, where the $2S$-$4S$ transition was detected both by the emitted Balmer-β fluorescence and the decrease in metastable flux on resonance, have been published in Ref. [12].

For the analysis of our experimental data, we first correct for a slow drift of the infrared laser's reference cavity. This drift causes a slow change of the frequency scan range of the infrared laser during the measurements. It is compensated for by observing the measured beat frequency between the doubled Ti:sapphire laser light and the blue light from the dye laser. We plot the temporal behavior of the beat frequency minus four times the drive frequency of the acousto-optic modulator which tunes the infrared laser frequency (AOM 2). Since the modulator is operated in double pass and the beat frequency is measured at twice the infrared frequency, we can display the frequency drift (a few kHz/min) of the infrared laser reference resonator as shown in Fig. 5. The resonator drift is fitted to a polynomial of up to fourth order using nonlinear regression. For further data analysis we use the analytical expression for the resonator frequency. We do this, first because frequency fluctuations of the blue dye laser due to the locking procedure to the $1S$-$2S$ signal are eliminated. Second, because we can interpolate over time periods in which the dye laser frequency lock to the $1S$-$2S$ signal was not sufficiently reliable due to vibrations of the cryopump evacuating the $1S$-$2S$ atomic beam apparatus. The cryopump is switched on automatically approximately every 10 minutes for about 2 minutes. The fit is done independently for the beat frequency data as measured by the spectrum analyzer and by the counter. We have varied the regression time interval and the order of the polynomial for testing purposes. The maximum difference of the interpolated beat frequencies as determined from the spectrum analyzer and from the counter was 4 kHz at 486 nm.

Next, we subdivide the data points—now corrected for the slow reference cavity drift—again into 100 or 200 frequency intervals (we use the average value of the beat frequency as derived by counter and spectrum analyzer) and average over the data in each of the frequency intervals. The uncertainty of the determination of the beat frequency is estimated to be 2.8 kHz using the independent frequency counter and spectrum analyzer measurements. Data points, where either the laser or the enhancement cavity frequency lock has failed (this can be detected by a lower transmission of reference or enhancement cavity), are discarded. After averaging, we obtain $2S$-$4S$ or $2S$-$4D_{5/2}$ spectra as discussed below.

B. Experimental spectra

Typical hydrogen $2S$-$4S$ and $2S$-$4D_{5/2}$ two-photon spectra fitted with theoretical lineshapes are shown in Fig. 6. These data have been recorded with the channeltron detector. The maximum signal decrease is about 5% for the $2S$-$4S$ and 20% for the $2S$-$4D_{5/2}$ transition. The latter transition is highly saturated especially for atoms which travel directly on the laser axis. Figure 7 shows typical hydrogen $2S$-$4S$ spectra observed by simultaneous detection of the blue Balmer-

β fluorescence and the decrease in metastable flux. For the fluorescence spectra, the signal at full laser power is about 300 counts/s on a background of 600 counts/s. Typical detection rates for the channeltron detector with the improved metastable source are 50 000 counted metastable atoms per second with a signal decrease of 2.5% on resonance. Thus the signal-to-nose ratio of the fluorescence signals is about a factor of 2 better than that of the corresponding channeltron signals, and could be further improved if the background radiation of the filament could be reduced.

The observed linewidths of the $2S$-$4S$ and $2S$-$4D_{5/2}$ transitions typically are about 1.5 and 7 MHz, corresponding to a resolution of 4 parts in 10^8 and 1 part in 10^8, respectively. The natural linewidths of the transitions are 0.704 and 4.36 MHz. The additional broadening is mainly due to saturation broadening and the ac Stark effect. The ac Stark effect not only shifts the line center but also broadens the lines due to the spatially inhomogeneous light intensity. The observed linewidth therefore increases with laser power.

The frequency axis in Figs. 6 and 7 refers to the measured beat frequency with the dye laser locked to the $1S$-$2S$ signal. Hydrogen and deuterium spectra of the $1S$-$2S$ transition are shown in Ref. [5]. Without Lamb shifts or relativistic effects the beat frequency on resonance would be exactly zero. In reality we observe a beat frequency of about 4.8 GHz for $2S$-$4S$ and 6.5 GHz for $2S$-$4D_{5/2}$ when the infrared laser is tuned to the line center. The $1S$ Lamb shift can be extracted from those spectra.

C. Calculation of theoretical line profiles

Since considerable light intensities are necessary for an observation of the weak $2S$-$4S$ and $2S$-$4D$ two-photon signals with a sufficiently good signal-to-noise ratio, saturation effects occur and the transition frequency is ac Stark shifted. For a typical optical power of 30 W per direction, the intensity on the beam axis reaches 8 kW/cm^2, which corresponds to an excitation rate of about 5000/s for the $2S$-$4S$ transition. The ac Stark shift of the $2S$-$4S$ line reaches about 500 kHz. Since this shift is linear in laser intensity, we can determine the unshifted center frequency to first order by recording spectra at different light intensities and simply extrapolating the line center to zero power. The expected line shapes however are slightly asymmetric and the ac Stark shift of the line center does not grow strictly linearly with laser power, since atoms that travel directly on the laser axis are already significantly depleted. Therefore we have fitted our spectra to theoretical line shapes which include saturation effects, the ac Stark shift and the second-order Doppler effect.

We start with a brief review of the theory of Doppler-free two-photon spectroscopy [42]. The atom absorbs two photons from opposite directions, each of them providing half of the energy necessary to excite the transition. The selection rules require $\Delta l=0$ or 2; for $\Delta l=0$ only $\Delta F=0$ and $\Delta m_F=0$ are observed. The excitation rate R_A in second-order perturbation theory for a transition from the initial state $|i\rangle$ to the final state $|f\rangle$ is [43]

$$R_A=\frac{I^2}{\varepsilon_0^2\hbar^4c^2}|M_{if}|^2\frac{\Gamma}{(2\omega-\omega_{fi})^2+(\Gamma/2)^2} \tag{7}$$

with

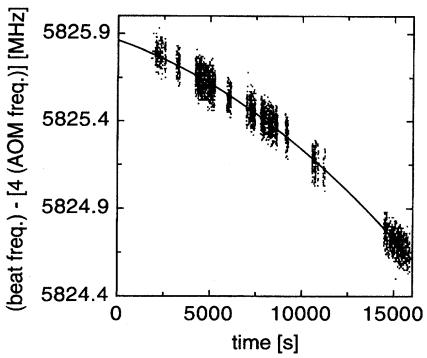

FIG. 5. Drift of the reference resonator (the beat frequency as determined by the spectrum analyzer subtracted by four times the drive frequency of AOM 2) vs time.

$$M_{if}=\sum_n \frac{\langle f|e\mathbf{r}\cdot\mathbf{p}|n\rangle\langle n|e\mathbf{r}\cdot\mathbf{p}|i\rangle}{\omega-\omega_{ni}},$$

$$|M_{if}|^2=\left(\frac{e^2a_0^2\hbar}{\alpha^2m_ec^2}\right)^2|\gamma|^2. \tag{8}$$

Here ω denotes the frequency, $\mathbf{p}$ the polarization, I the intensity of the exciting light field per direction, Γ the linewidth of the transition, and $\omega_{fi}=(E_f-E_i)/\hbar$ the atomic transition frequency. The sum in the expression for the matrix element M_{if} of all possible intermediate states $|n\rangle$ includes the bound P states and the continuum states, for which the sum has to be replaced by an integral. γ is the value of the matrix element M_{if} in atomic units.

At high light intensities, the atomic transition frequency is shifted: $\omega_{fi}=\omega_{fi}(0)+c_{ls}I$, where the coefficient of the light shift c_{ls} is

$$c_{ls}=\left(\frac{4\pi a_0^2}{m_ec^2\alpha}\right)(\beta_i-\beta_f), \tag{9}$$

with $\beta_k(k=i,f)$ as (in atomic units)

$$\beta_k=\sum_n\left(\frac{\langle k|z|n\rangle^2}{E_k-E_n+\omega}+\frac{\langle k|z|n\rangle^2}{E_k-E_n-\omega}\right). \tag{10}$$

The coefficients γ and β, and the natural linewidths $\Gamma_{\rm nat}$ are given in Table III for the transitions $1S$-$2S$, $2S$-$4S$, and $2S$-$4D$.

Taking into account ac Stark shift and also the second-order Doppler effect but still neglecting saturation, we obtain the following expression for the excitation rate with $\Omega=2\omega-\omega_{if}(0)$ as the laser detuning:

$$R_A=k_AI^2\frac{\Gamma}{[\Omega-c_{ls}I+\frac{1}{2}(v/c)^2\omega_{fi}]^2+(\Gamma/2)^2}, \tag{11}$$

where $k_A=(4\pi a_0^2/mc^2\alpha)^2\ |\gamma|^2\ C_{\rm FS}$. The constant $C_{\rm FS}$ accounts for the distribution of the oscillator strength due to the excited state fine structure. $C_{\rm FS}$ is equal to 1 and 0.6 for $2S$-$4S$ and $2S$-$4D_{5/2}$, respectively, according to the statisti-

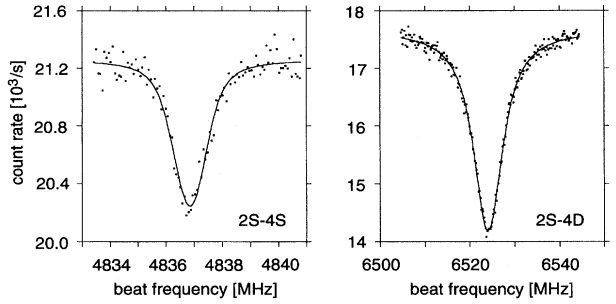

FIG. 6. Hydrogen two-photon spectra of the transitions $2S_{1/2}(F=1)$-$4S_{1/2}(F=1)$ (left, light power $P=40$ W) and $2S_{1/2}(F=1)$-$4D_{5/2}$ (right, $P=25$ W). The quoted beat frequency has been measured with the dye laser locked to the $1S_{1/2}(F=1)$-$2S_{1/2}(F=1)$ transition.

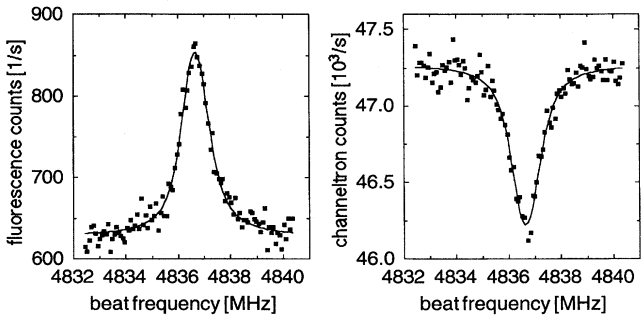

FIG. 7. Hydrogen two-photon spectra of the transitions $2S_{1/2}(F=1)$-$4S_{1/2}(F=1)$ at a light power of 31 W, simultaneously detected by Balmer-β fluorescence (left) and by decrease of metastable $2S$ signal (right). The quoted beat frequency has been measured with the dye laser locked to the $1S_{1/2}(F=1)$-$2S_{1/2}(F=1)$ transition.

cal weights. Note that the units of ω_{fi} and Γ are angular frequencies, while we obtain R_A in Hz.

The complete pump scheme for the two-photon transitions including all relevant hyperfine states is shown in Fig. 8 for $2S(F=1)$-$4S(F'=1)$. Initially the metastable $2S$ atoms populate the two hyperfine levels $F=0$ and $F=1$ (deuterium: $F=\frac{1}{2}$ and $F=\frac{3}{2}$) according to their statistical weights. The statistical weight of $F=1$ is $C_{\rm HFS}=\frac{3}{4}$ (deuterium $F=\frac{3}{2}$ level: $C_{\rm HFS}=\frac{2}{3}$). The excited $4S$ and $4D$ states rapidly decay via either the $3P$ or the $2P$ intermediate level mainly into the $1S$ ground state. From the $3P$ state there is a decay channel back into both of the $2S$ hyperfine levels. The repumping probabilities p_i into $2S(F_i)$ for an atom initially excited from $2S(F=1)$ into $4S$ and $4D_{5/2}$ are given in Table IV.

We first describe the calculation of the Balmer-β fluorescence signal. Since we have used the fluorescence detector only for the $2S$-$4S$ signals, we now concentrate on this transition. The lifetime of the unperturbed $4S$ level is $\tau=226$ ns [36]; the probability for a decay into $2P$ is $\rho=58\%$ during which a blue fluorescence photon at 486.3 nm is emitted. Since the binding energy of the $4S$ state is only $-hcR_\infty/16$, the atom is ionized by absorption of a further 972-nm photon. Due to the high intensity of the infrared light used in our experiment, the ionization rate $R_i(I)$ is comparable to the spontaneous decay rates $R_3=(1-\rho)/\tau$ and $R_2=\rho/\tau$ into the $3P$ and $2P$ states and thus cannot be neglected:

$$R_2=2.56\times10^6/\text{s},$$

$$R_3=1.85\times10^6/\text{s},$$

$$R_i(I)=I\times0.01579\ \ \text{m}^2/\text{W s}.$$

The linewidth Γ of the transition is increased by ionization: $\Gamma(I)=R_{\rm tot}(I)=R_2+R_3+R_i(I)$. At maximum power typically 20% of the atoms which are excited into the $4S$ state will ionize. For the ionization cross section of the $4S$ state at 972 nm we use the value $\sigma=1.613\times10^{-17}$ cm^2 [36,46].

The probability for an atom initially in $2S_{1/2}(F=1)$ to be excited into $4S_{1/2}(F=1)$ and to emit a blue fluorescence photon during the decay from $4S$ can be calculated by solving the rate equations. We have obtained the following expression for the probability $F(0,T)$ of this decay during the time interval 0 and T:

$$F(0,T)=\int_0^T dt\,\frac{R_2}{R_{\rm tot}(t)}\,R_A(t)\times\exp\left[-\int_0^t dt'\left(1-p_1\frac{R_2+R_3}{R_{\rm tot}(t')}\right)R_A(t')\right]. \tag{12}$$

Along its trajectory, the atom experiences a time-dependent light intensity. We convert the time integrations into line integrals along the trajectory of the atom traveling through the light field with velocity v. Next we average over the velocity distribution of the flux $f(v)\propto v^4\exp(-v^2/v_0^2)$ of the metastable atomic beam (Sec. III B 2).

For a systematic treatment of the possible atomic trajectories through the light field, we assume the starting point of a trajectory on a first aperture of radius r_{m1} directly behind the metastable source. The end point is on a second aperture with radius r_{m2} after an interaction region of length L. Due to the cylindrical symmetry, a trajectory is characterized by only three variables r_1, r_2, and Θ, where r_1 and r_2 denote the distance of the trajectory to the axis on the first and second aperture, respectively, and Θ ($\Theta_2-\Theta_1$) is the relative angle between the intersections on the apertures. A typical atomic trajectory through the light field is shown in Fig. 9. The infrared standing wave has a Gaussian intensity distribution in transverse direction. The atom experiences a laser intensity that is determined by the distance $r(z)$ to the axis

$$I(z)=I_0\exp\left[-2\left(\frac{r(z)}{w(z)}\right)^2\right]. \tag{13}$$

The waist of the laser beam $w(z)$ is determined by the geometry of the optical resonator (Sec. III B 3) [47]. The fluorescence detector can detect Balmer-β photons which are emitted in the region $l\leq z\leq L$. The probability F_Ω^i for a trajectory i to contribute to the fluorescence signal for a detuning Ω is

TABLE III. Natural linewidth Γ_{nat}, matrix element γ, and coefficient of light shift β for some transitions of interest.

Transition	γ (atomic units)	β (atomic units)	$\Gamma_{nat}/2\pi$ (kHz)
$1S$-$2S$	7.85[a]	35.57[b]	0.0013[c]
$2S$-$4S$	16.63[d]	653.90[d]	706
$2S$-$4D$	−213.54[d]	732.98[d]	4360

[a]Reference [44].
[b]Reference [45].
[c]Reference [36].
[d]Reference [43].

$$F_\Omega^i = \int_v dv\, f(v)\frac{1}{v}\int_l^L dz\, \frac{R_2}{R_{tot}(I(z))} \times \frac{k_A\Gamma(I(z))I^2(z)}{[\Omega - c_{ls}I(z) + \frac{1}{2}(v/c)^2\omega_{fi}]^2 + \left(\frac{\Gamma(I(z))}{2}\right)^2} \times \exp\left[-\frac{1}{v}\int_0^z dz' \left(1 - p_1 \frac{R_2+R_3}{R_{tot}[I(z')]}\right) \right] \times \frac{k_A\Gamma(I(z'))I^2(z')}{[\Omega - c_{ls}I(z') + \frac{1}{2}(v/c)^2\omega_{fi}]^2 + \left(\frac{\Gamma(I(z'))}{2}\right)^2} \Bigg]. \quad (14)$$

For a calculation of the theoretical line shapes, we have to sum the contributions of all possible atomic trajectories to the signal. We use a numerical Monte Carlo method and assume an equal distribution of the start and end points over both apertures. The parameters r_1 and a point on the exit aperture are chosen randomly and independently from each other. For each trajectory selected in this way F_Ω^i is calculated by numerical integration in v, z, and z'. The fraction of atoms F_Ω which emit a fluorescence photon in the detection region is given by the weighted sum of F_Ω^i of the randomly selected trajectories

$$F_\Omega = C_{HFS}\frac{\sum_i g^i F_\Omega^i}{\sum_i g_i}, \quad (15)$$

where $g_i = 2\pi r_l$ is the weighting factor for a trajectory. A typical value for F_Ω in the line center is 0.31% for trajectories with $r_{m2}=2$ mm and for 30 W infrared light power ($r_{m1}=2$ mm, $w_0=0.38$ mm, $L=330$ mm). Sufficient convergence is obtained when summing the contributions of 200 000 trajectories for each of 91 equally distributed frequency points Ω. The line center then converges to 10^{-3} of the linewidth.

The calculation of the expected $2S$-$4S$ line shape for the channeltron signal is analogous to that for the fluorescence signal. For the decrease in population of the $2S$ state we obtain for a transition starting from $2S(F=1)$:

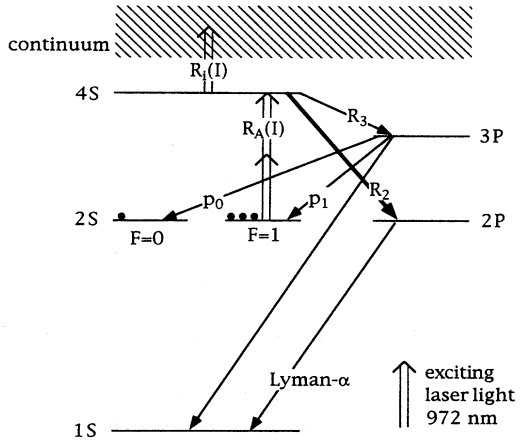

FIG. 8. Complete pump scheme for the $2S_{1/2}(F=1)$-$4S_{1/2}(F=1)$ two-photon transition in atomic hydrogen.

$$S_\Omega^i = \int_v f(v)dv\left(1 - \frac{p_0}{1-p_1}\right)\Bigg[1 - \exp\Bigg(-\frac{1}{v}\int_0^L \times \frac{(1-p_1)k_A\Gamma(I(z))I^2(z)}{[\Omega - c_{ls}I(z) + \frac{1}{2}(v/c)^2\omega_{fi}]^2 + \left(\frac{\Gamma(I(z))}{2}\right)^2} dz \Bigg)\Bigg]. \quad (16)$$

This formula accounts for the fine and hyperfine structure of the levels and also for the repopulation of the $2S$ state described by the probabilities p_1 and p_0, as shown in Fig. 8. Note that for the channeltron signal the total interaction length of atoms and light field contributes, and we have to take into account repumping into $2S(F=0)$. For a deuterium transition starting from $2S_{1/2}(F=\frac{3}{2})$, the factors p_0 and p_1 are replaced by $p_{1/2}$ and $p_{3/2}$, respectively. Ionization has a negligible effect on the channeltron signals, since it affects only a small fraction of atoms (4.2%) which are repumped into the $2S_{1/2}(F=1)$ state (for deuterium: 2.4%).

The numerical calculations were done on a SPARC 10 workstation, where the calculation time was approximately 10 h per lineshape. Figure 10 shows three theoretical $2S$-$4S$ line profiles for different laser powers, which predict the signal as detected by the fluorescence detector. The ac Stark shift of the line, the increase in linewidth due to ionization at higher laser powers, and saturation can clearly be observed.

TABLE IV. Probabilities p_i for optical pumping back into the two hyperfine levels i of the $2S$ state for an atom initially excited from $2S(F=1)$ in hydrogen and $2S(F=\frac{3}{2})$ in deuterium into $4S_{1/2}$ and $4D_{5/2}$ by two-photon spectroscopy (see also Fig. 8). $R_s=0.049\,21$, $R_d=0.030\,11$ [43].

	Hydrogen		Deuterium	
Transition	p_0	p_1	$p_{1/2}$	$p_{3/2}$
$2S_{1/2}$-$4S_{1/2}$	$4/27\times R_s$	$23/27\times R_s$	$16/81\times R_s$	$65/81\times R_s$
$2S_{1/2}$-$4D_{5/2}$	$2/15\times R_d$	$13/15\times R_d$	$8/45\times R_d$	$37/45\times R_d$

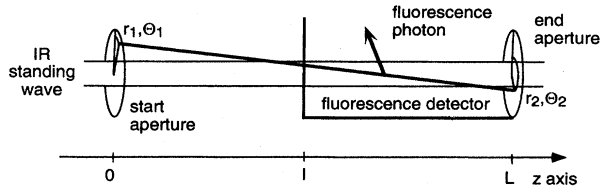

FIG. 9. Atomic trajectory through the infrared standing wave.

The calculated line profiles were fitted to our latest experimental fluorescence and channeltron $2S$-$4S$ spectra. In our first and second group of measurements we have recorded $2S$-$4S$ and $2S$-$4D$ spectra with the channeltron detector. To analyze these spectra, theoretical line profiles were calculated using a full integration method, as described by Garreau *et al.* [43]. The decrease in the count rate of metastable $2S$ atoms was computed by numerically calculating the integral over all atomic trajectories:

$$S_\Omega = C_{\rm HFS}\frac{4}{\pi r_{m1}^2 r_{m2}^2}\int_0^{r_{m1}} dr_1 r_1 \int_0^{r_{m2}} dr_2 r_2 \times \int_0^{\pi} d\theta\, S_\Omega(r_1,r_2,\theta). \quad (17)$$

Since we only recorded the decrease in metastable signal, it was not necessary to include ionization. To save computation time, we did not carry out the integration over the atomic velocity distribution. Instead we assumed a mean atomic velocity $v_{\rm IM}=\langle 1/v\rangle^{-1}=\frac{3}{4}\sqrt{\pi}v_0$ for all the atoms. In the limit of low light powers the obtained expression is exact. The second-order Doppler effect was accounted for by calculating the overall shift of the line center instead of adding the Doppler shift to the laser detuning in the expression for the excitation rate. This is justified by the fact that the second order Doppler sift is much smaller than the natural linewidth. The resulting shift of the line center can approximately be derived by the following integral for a velocity distribution of the flux $f(v)\propto v^4\exp(-v^2/v_0^2)$, if we assume an excitation rate proportional to $1/v$:

$$\Delta\nu_d = \frac{\nu_{if}}{2c^2}\frac{\int_0^\infty v^5\exp(-v^2/v_0^2)dv}{\int_0^\infty v^3\exp(-v^2/v_0^2)dv}. \quad (18)$$

We obtain the average second-order Doppler shifts as given in Table V. The broadening of the line due to the velocity distribution is of the same order of magnitude. In order to verify whether this approximation is still correct for higher laser powers where saturation is significant, the resulting line shape was compared with the exact calculation for one example [43]. The relative frequency error turned out to be about 10^{-13}, which may be neglected.

D. Fit with the calculated line shapes

In the preceding section, we described how the theoretical $2S$-$4S$ and $2S$-$4D$ line shapes were calculated. Additional broadening mechanisms such as laser frequency or intensity fluctuations and stray electric fields have been accounted for by convolution of the theoretical line shapes with a Gaussian profile. We have fitted the theoretical line shapes to the experimental spectra by using a Levenberg-Marquard algorithm [48]. Due to the long computation time which is necessary for the theoretical line profiles it is not possible to solve the multidimensional calculation during each step of the fit procedure. We have calculated the theoretical line profiles for several laser powers from 5 to 50 W in steps of 5 W and as a function of laser detuning in steps of 100 kHz ($2S$-$4S$) and 500 kHz ($2S$-$4D$). During the fitting procedure we interpolate between these points quadratically in frequency and cubic in laser power. The quality of this interpolation was estimated by doubling the lattice spacing to be better than 0.1%. The whole fitting procedure is designed to correct for the ac Stark effect.

1. Channeltron signals

We fit the theoretical line shapes to the experimental $2S$ quench signals using the metastable flux, the corrected center frequency, the laser power, and the Gaussian broadening as adjustable fit parameters. A backup value for the light power is obtained from a photodiode mounted behind the slightly transmitting end mirror of the enhancement cavity. The fitting procedure used for channeltron signals is very similar to that described in Ref. [43]. Figure 11 shows the calculated center frequency as generated by the fit plotted versus the photodiode signal for all atomic spectra taken during one day of measurement. The upper curve, for comparison, gives the shift of the line center as a function of power. The shift at maximum intracavity laser power (about 30 W) is about 600 kHz. By fitting the experimental spectra with calculated line shapes the bulk of the ac Stark shift can be corrected as shown in the lower curve of Fig. 11. To correct for a slight residual dependence of the fitted center frequency on light intensity, we take spectra for different laser powers and extrapolate to zero power.

We note that for the first and second group of measurements using the first version of the metastable beam source we observed a variation of the fitted center frequency on laser power of approximately 10% of the shift of the line center, when we assumed the effective radius of the aperture of the metastable atomic beam to be equal to the geometrical one (2 mm). We believe that this was due to a spatially inhomogeneous distribution of the electron current causing a smaller effective aperture of the metastable beam. When we assumed an effective radius of 1.25 mm for the radius of the first aperture, the extrapolation line was horizontal within the errors bars. For the third set of data using the newer version of the metastable source with three filaments, the effective radius was comparable to the geometrical radius of 2 mm. Mainly in our earlier data sets we also had the problem that we could not measure the dark count rate directly. In our initial measurements a residual electric field in the channeltron detector quenched about 25% of the metastable flux even when no quench voltage was present [11]. By coating all metal parts in the detector with graphite, we have reduced this fraction to an estimated fraction of 3%. We estimate the actual dark count rate by a comparison of the signal saturation with and without applied quench voltage [41]. When varying the true dark count rate from the estimated rate of typically 1800/s to zero, the extrapolated beat frequency

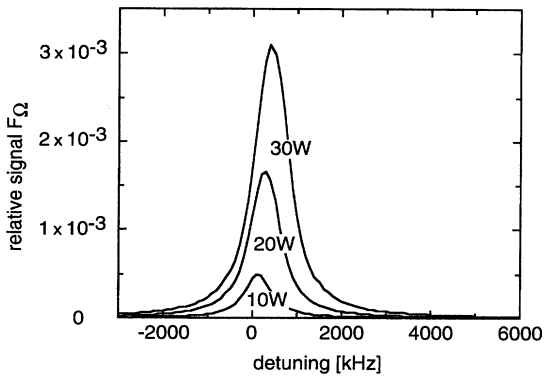

FIG. 10. Three theoretical fluorescence signal line profiles of the $2S_{1/2}(F=1)$-$4S_{1/2}(F=1)$ two-photon transition in atomic hydrogen for different light powers.

changes by less than 1 kHz for the latest data, which will be accounted for in the determination of the systematic errors.

As a further test of the fitting procedure, we have compared the light power as generated by the fit procedure with the photodiode signal. Although we cannot determine the absolute intracavity power with the photodiode to better than a few percent, we can monitor the proportionality of calculated and measured power. To account for a slight nonlinearity, we have performed the extrapolation of the measured beat frequency to zero power not only using the photodiode signal, but also using the power derived from the fit program. The difference between both results was 5 kHz for hydrogen and 0.3 kHz for deuterium for our latest set of data. For determination of the $1S$ Lamb shift we have used the average of both extrapolation results. We estimate the systematic error of the fitting procedure for the averaged result quoted below (the latest data set) by dividing the differences by $\sqrt{2}$ and adding the quoted variation of the fitted center frequency on the estimated dark count rate.

2. Fluorescence signals

Whereas for the channeltron signals the fit program could derive the light power from the saturation of the signal, the percentage of atoms excited into $4S$ cannot *a priori* be derived precisely from the fluorescence signals, since it involves the detector quantum efficiency. We use two different methods for the data analysis. For the first method, we assume the intracavity light power to be known, being proportional to the measured transmitted power of the enhancement cavity. The proportionality constant is derived from the requirement that the fitted center frequency is independent of the light power for all spectra taken during one day of measurement. We fit the theoretical line shapes to the fluorescence signals by using background count rate, quantum efficiency of the detector multiplied by the metastable flux, Gaussian broadening, and corrected center frequency as adjustable fit parameters.

For the second fitting method, we assume the detector quantum efficiency to be known. Using the metastable flux determined from the channeltron signals we then can derive the signal saturation. The detector quantum efficiency is determined from the requirement, that the fitted center frequency is independent of the laser power for all spectra taken during one day of measurement. As in the case of the channeltron signals we now use the light power as a fourth fitting parameter.

The difference in the derived center frequencies between both fitting methods was 5.7 and 6.5 kHz at 486 nm for hydrogen and deuterium, respectively. For further analysis we use the average of both results. We estimate the systematic error of the fitting procedure for the averaged result by accounting for this difference and adding a typical variation of the result (about 3 kHz) on the assumed constant for each of the methods.

V. RESULTS

A. Determination of the atomic $(E_{4S,4D}$-$E_{2S})$-$\frac{1}{4}(E_{2S}$-$E_{1S})$ difference frequency

We describe here the determination of the atomic difference frequencies $(E_{4S,4D}$-$E_{2S})$-$\frac{1}{4}(E_{2S}$-$E_{1S})$ from our experimental results. We have performed the extrapolation of the measured beat frequencies for the channeltron and fluorescence data separately for every day of data taking. The averaged results ($2S$-$4S$) for our latest data set are given on top of Table V. Several corrections are applied, in addition to the corrections for the line shape and the reference cavity drift already discussed in previous sections.

1. Second-order Doppler shift

We have measured the velocity distribution of both atomic beams by excitation of the Doppler broadened $2S$-$4P$ transition. For the $1S$ ground state beam of the $1S$-$2S$ spectrometer, we obtained a most probable velocity of the flux of 950(120) m/s for hydrogen and 670(90) m/s for deuterium for a cooling of the beam to liquid nitrogen temperature. The corresponding second-order Doppler shift is given in Table V and represents the largest uncertainty associated with the $1S$-$2S$ spectrometer.

For the metastable beam of the $2S$-$4S$ spectrometer, we obtained the atomic velocities given in Sec. III B 2. As described previously, we have accounted for the second-order Doppler shift of the $2S$-$4S$ transition in the calculations of the theoretical line shapes for our latest data set. For clarity in Table V we give the mean second-order Doppler shifts, which are calculated as described in Sec. IV C.

2. Zeeman shift

In the $1S$-$2S$ spectrometer magnetic fields cause a second-order Zeeman shift. Assuming an equal initial population of all m_F levels, the shift of the line center is 0.804 kHz/G^2 at 486 nm for the hydrogen $1S(F=1)=2S(F=1)$ transition, which can be neglected [5]. For deuterium the Zeeman shift is larger due to its smaller hyperfine structure. By applying a magnetic field of a few Gauss, we separate the second-order magnetic field sensitive $1S(F=3/2),m_F=\pm 1/2$-$2S(F=3/2),m_F=\pm 1/2$ transition from the field insensitive $F=3/2,m_F=\pm 3/2$ components, and only excite the latter transition.

In the $2S$-$4S$,$4D$ spectrometer, magnetic fields broaden the $2S$-$4D$ resonance. For the first and second group of mea-

TABLE V. Calculation of the hydrogen $(E_{4S}-E_{2S})-\frac{1}{4}(E_{2S}-E_{1S})$ atomic transition frequency from the measured beat frequencies (third data set only).

	Hydrogen		Deuterium	
	fluorescence signal (MHz)	channeltron signal (MHz)	fluorescence signal (MHz)	channeltron signal (MHz)
Extrapolated beat frequency	4836.137(10)	4836.146(15)	4813.660(12)	4813.586(28)
Corrections:				
line shape	0.000(5)	0.000(5)	0.000(5)	0.000(1)
second-order Zeeman shift	−0.005(3)	−0.005(2)	−0.032(16)	−0.029(15)
dc Stark effect	0.000(2)	0.000(0)	0.000(2)	0.000(0)
Corrected beat frequency	4836.132(12)	4836.141(16)	4813.627(21)	4813.557(32)
Averaged corrected beat frequency	4836.135(9)		4813.616(20)	
Reference cavity drift	0.000(3)		0.000(3)	
Second-order Doppler shift				
$1S$-$2S$ (80 K line)	−0.003(1)		−0.002(0)	
$2S$-$4S$	0.046(4)		0.015(2)	
Hyperfine structure	−38.838(0)		−11.935(0)	
$(E_{4S}-E_{2S})-\frac{1}{4}(E_{2S}-E_{1S})$ (hyperfine centroid)	4797.340(10)		4801.694(20)	

surements we have shielded magnetic fields in the interaction region of the $2S$-$4S$,$4D$ spectrometer with a Mu-metal tube. The residual field was measured to be below 10 mG within 4/5 of the interaction length, corresponding to a broadening of approximately 100 kHz. For the $2S$-$4S$ transition there is only a second-order Zeeman shift. The shift of the line center is 25.72 kHz/G^2 for the $2S(F=1)$-$4S(F=1)$ line of hydrogen, and 167.39 kHz/G^2 for $2S(F=3/2)$-$4S(F=3/2)$ in deuterium. In our latest measurements the Mu-metal shield was removed in order to detect the atomic resonance via the blue Balmer-β fluorescence. After completion of the measurements, we discovered that the residual inhomogeneous magnetic field was larger than expected. We have measured the magnetic field along the beam axis (about 400 mG rms) and performed a numerical Monte-Carlo calculation (similar to that described in Sec. IV C, however neglecting signal saturation). We are summing the contribution of all possible atomic trajectories to compute the second-order Zeeman shift of the atomic resonances. The results are given in Table V, especially for deuterium the shift is significant due to is small $4S$ hyperfine structure.

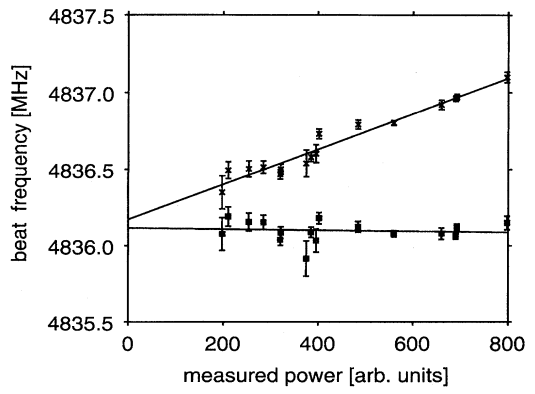

FIG. 11. Dependence of the fitted center frequency (■) and the line center (×) on light power for channeltron data.

3. dc Stark effect

We estimate residual stray electric field in the excitation region to be less than 50 mV/cm for the channeltron signal and negligible (<10 mV/cm) for the fluorescence signal due to the large distance of the observed atoms from the electron gun. The corresponding uncertainties for the channeltron signals are 1.5 kHz for $2S$-$4S$ and 3 kHz for $2S$-$4D_{5/2}$.

4. Hyperfine structure

For the hyperfine structure of the $1S$-$2S$ states we use published experimental values [49]. For that of the $4S$ and $4D$ states we use values extrapolated from the $1S$ level. In the nonrelativistic limit the state dependence of the hyperfine energy is described by the Fermi formula. The largest state dependent correction to this formula is a relativistic correction to the probability of the electron being at the nucleus of order $(Z\alpha)^2$ [19,50]. Including this correction, the hyperfine energy for S states is given by

$$E_{\mathrm{HFS}}=E_{\mathrm{Fermi}}\left\{1+(Z\alpha)^2\left[\frac{11}{6}\left(1-\frac{1}{n^2}\right)+\frac{3}{2n}\right]\right\}, \quad (19)$$

where E_{Fermi} (proportional to $1/n^3$) denotes the hyperfine energy as given by the Fermi formula. The relativistic correction has been derived by Breit for $n=1$ and 2 [51]. Accounting for this correction, we can determine the hyperfine

energy for all hydrogen S-states to a precision of some parts in 10^6. The obtained hyperfine splittings for $4S_{1/2}$ and $4D_{5/2}$ are given in Table VI.

For the $2S$-$4D_{5/2}$ line we simultaneously excite transitions to several $4D_{5/2}$ hyperfine substates, since the hyperfine structure of the $4D_{5/2}$ state is smaller than its natural linewidth. The hyperfine structure of the $2S$ initial state however is resolved, and we start from a distinct $2S$ hyperfine level. Therefore for the $2S(F)$-$4D_{5/2}$ line a correction is necessary which takes into account the relative excitation probabilities [43]. For example, the relative excitation probability from $2S(F=1)$ to $4D_{5/2}(F=2)$ is $\frac{2}{9}$, whereas to $4D_{5/2}(F=3)$ it is $\frac{7}{9}$, which does not correspond to the statistical weights. The corresponding shift of the line center is 222.0 kHz for hydrogen and 68.2 kHz for deuterium.

5. *Results of the frequency comparison*

If we average our latest results from fluorescence and channeltron detection, we obtain the atomic $(E_{4S}-E_{2S})-\frac{1}{4}(E_{2S}-E_{1S})$ difference frequencies listed at the bottom of Table V. For our first two data sets we also have compared $1S$-$2S$ with $2S$-$4D_{5/2}$. The obtained difference frequencies of the hyperfine centroids were $(E_{4S}-E_{2S})-\frac{1}{4}(E_{2S}-E_{1S})$: 4797.322(25) MHz and 4801.674(74) MHz, $(E_{4D_{5/2}}-E_{2S})-\frac{1}{4}(E_{2S}-E_{1S})$: 6490.144(24) MHz and 6494.841(41) MHz for hydrogen and deuterium, respectively [31,41].

The weighted average of all data sets for the atomic difference frequencies $(E_{4S,4D}-E_{2S})-\frac{1}{4}(E_{2S}-E_{1S})$ are given in the second line of Table VII (these values will be used for determination of the $1S$ Lamb shifts). These results are the most precise ones today. They are in agreement with the theoretical values given in the first line, which were obtained assuming a proton charge radius $r_p=0.862(12)$ fm as measured by Simon *et al.* [10].

B. Lamb shift

After these corrections, we can determine the $1S$ Lamb shift from the measured difference frequencies:

$$\Delta=(E_{4S,4D}-E_{2S})-\tfrac{1}{4}(E_{2S}-E_{1S})$$
$$=\Delta_{\mathrm{DC}}+\Delta_{\mathrm{RM}}+\tfrac{1}{4}L_{1S}-\tfrac{5}{4}L_{2S}+L_{4S,4D}, \qquad (20)$$

where L denotes the Lamb shift of the corresponding state. Dirac and reduced mass corrections are contained in Δ_{DC} and Δ_{RM}. As the simple Bohr model suggests, the bulk of the energy contributions in Δ_{DC} and Δ_{RM} scales as $1/n^2$ and thus cancels. The deviations from this simple scaling law are mainly due to relativistic effects, which are small and well known. After taking them into account, we obtain a compound "hyper-Lamb-shift" $\frac{1}{4}L_{1S}-\frac{5}{4}L_{2S}+L_{4S,4D}$ (Table VII). Since quantum electrodynamic and nuclear size effects scale with the principle quantum number n approximately as $1/n^3$, the $1S$ Lamb shift is the largest in hydrogen. Using the experimental value for the $2S$-$2P$ Lamb shift in hydrogen and the theoretical values for the smaller Lamb shifts of the states $2P$ and $4S$ in hydrogen and $2S$ and $4S$ in deuterium (Table I) we can determine the $1S$ Lamb shift. For the hydrogen $2S_{1/2}$-$2P_{1/2}$ Lamb shift we take the value 1057.845(9) MHz obtained by Lundeen and Pipkin using radio frequency measurements [2].

Our result for the $1S$ Lamb shift is $L_{1S}=8172.874(60)$ MHz for hydrogen and $L_{1S}=8183.807(78)$ MHz in deuterium [53]. Contributions to the total uncertainties are summarized in Table VIII and a comparison with other recent measurements of the $1S$ Lamb shift is given in Table IX. Our results are in agreement with those of earlier work, and are currently the most precise. Figure 12(a) compares our result for hydrogen with the theoretical predictions with and without recently calculated two-loop binding corrections [9]. Including these corrections the agreement between theory and experiment is good, while it is not satisfactory neglecting these corrections, as was noted previously [12]. We base the theoretical predictions on a proton charge radius as measured by Simon *et al.* [10] [$r_P=0.862(12)$ fm], which is believed to be more reliable than an older measurement [$r_P=0.805(11)$ fm] [52] since data points were taken at lower electron-proton momentum transfers reducing the effects of disturbing mesonic and quark resonances. Assuming the older value for the proton charge radius the theoretical value decreases by 149 kHz, lessening the agreement between theory including two-loop binding corrections and experiment (while the agreement between theory based on the old proton charge radius and without two-loop binding corrections is satisfactory). Improvements in the measurement of the proton charge radius are highly desirable for a more critical comparison between experiment and quantum electrodynamic theory on bound systems, and should be possible by a Lamb shift measurement in muonic hydrogen [56].

For the hydrogen $2S$ Lamb shift, theory including two-loop binding corrections is also in agreement with experiments, as shown in Fig. 12(b). However there now is a disagreement of five combined standard deviations between the theoretical value for the $2S$ Lamb shift of He^+ and measurements based on quench asymmetry [15].

C. Isotope shifts

The isotope shift of the atomic energy levels (corrected for hyperfine structure) between hydrogen and deuterium is due to the difference in nuclear masses and sizes of the isotopes. For an nS state, the isotope shift of the hyperfine centroid is

$$\delta=[E_{\mathrm{RM}}(H)+E_{\mathrm{LS}}(H)]-[E_{\mathrm{RM}}(D)+E_{\mathrm{LS}}(D)]$$
$$=\frac{R_\infty c}{n^2}\frac{1-m_p/m_d}{m_p/m_e}+S_r-\frac{1}{n^3}\left(\frac{4\alpha^4 R_\infty c}{3r_e^2}(r_{\mathrm{ch},d}^2-r_{\mathrm{ch},p}^2)\right), \qquad (21)$$

where S_r contains well-known terms such as reduced mass corrections higher order in m_e/m_p, recoil terms of the Lamb shift, and corrections due to the nuclear polarizabilities. From our measured isotope shift of $(E_{4S,4D}-E_{2S})-\frac{1}{4}(E_{1S}-E_{2S})$ we can, since terms scaling as $1/n^2$ are eliminated, determine the difference of the deuteron and proton nuclear charge radii: $r_{\mathrm{ch},d}^2-r_{\mathrm{ch},p}^2=3.70(11)$ fm^2. Using Eq. (6), we can replace $r_{\mathrm{ch},d}^2-r_{\mathrm{ch},p}^2$ by $r_{E,d}^2+r_n^2+3\hbar^2/4m_p^2c^2$ and determine the deuteron matter radius using the neutron charge radius. Our result for the deuteron matter radius is $r_{E,d}=1.945(28)$ fm.

TABLE VI. Hyperfine splittings of the states $1S$, $2S$, $4S$, and $4D_{5/2}$ in hydrogen and deuterium.

State	Hydrogen (MHz)	Deuterium (MHz)
$1S_{1/2}$	1420.405 751 766 7(9)	327.384 352 521 9(17)
$2S_{1/2}$	177.556 86(5)	40.924 439(20)
$4S_{1/2}$	22.194 54(11)	5.115 54(3)
$4D_{5/2}$	1.1414(1)	0.1462[a]
		0.2046[b]

[a]For $F=3/2$-$F=5/2$.
[b]For $F=5/2$-$F=7/2$.

Recently the hydrogen deuterium isotope shift of $1S$-$2S$ has been measured to be 670 994.337(22) MHz [16]. This shift potentially can be measured extremely precisely due to the small natural linewidth of $1S$-$2S$. There are two possible interpretations of this measurement. First, combining this result with our measured isotope shift of $(E_{4S,4D}-E_{2S})-\frac{1}{4}(E_{1S}-E_{2S})$ we can eliminate both terms scaling as $1/n^2$ and $1/n^3$ in the isotope shift [see Eq. (21)] and simultaneously determine the electron proton mass ratio and nuclear size or structure effects. We derive an electron proton mass ratio of $m_e/m_p=1/1836.153\ 12(40)$. which is in fair agreement with the much more precise value $m_e/m_p=1/1836.152\ 664\ 6(58)$ obtained by van Dyck *et al.* via mass spectroscopy in a Penning trap [26].

A second interpretation of the result for the isotope shift of $1S$-$2S$ using the electron proton mass ratio measured by van Dyck *et al.* yields a very precise determination of the deuteron matter radius [22]. Especially due to the latest refinements of Penning trap mass spectroscopy this interpretation may seem more reasonable. From the isotope shift of $1S$-$2S$ we derive $r^2_{\mathrm{ch},d}-r^2_{\mathrm{ch},p}=3.822(16)$ fm^2, and from that a deuteron matter radius $r_{E,d}=1.977(4)$ fm (this value differs slightly from that given in Ref. [22] due to the new value for m_e/m_p and the improved recoil corrections [20] to the Lamb shift).

While the deuteron matter radius determined from the isotope shift of $(E_{4S,4D}-E_{2S})-\frac{1}{4}(E_{2S}-E_{1S})$ is in agreement with the radius obtained in an analysis of low energy electron scattering data [$r_{E,d}=1.953(3)$ fm] [23], the more precise value determined from the isotope shift of $1S$-$2S$ disagrees with the electron scattering result by 4.6 combined standard deviations. A more recent electron scattering experiment using higher momentum transfer suggests the larger value $r_{E,d}=1.964(7)$ fm [57], which is in better agreement with the radius determined from the isotope shift of $1S$-$2S$. Theoretical nuclear models also seem to favor a larger value for the deuteron matter radius. Friar *et al.* obtained a theoretical value $r_{E,d}=1.968(1)$ fm [58], which is not compatible with earlier electron scattering data [23] but is in better agreement with the deuteron matter radii extracted from both of our isotope shift measurements.

D. Rydberg constant

The absolute frequency of the $1S$-$2S$ transition has recently been determined with a phase locked frequency chain [13]. Applying our measured ground state Lamb shifts, we can determine the Rydberg constant from the measured 2 466 061 413.182(45) MHz for the hyperfine centroid of the hydrogen $1S$-$2S$ transition frequency. The result [59] is $R_\infty=109\ 737.315\ 684\ 9(30)$ cm^{-1} corresponding to a precision of 2.7 parts in 10^{11}, which is in agreement with the value given by Nez *et al.* [14] $R_\infty=109\ 737.315\ 683\ 4(24)$ cm^{-1}.

VI. CONCLUSIONS

By means of a direct comparison of the hydrogen $1S$-$2S$ with the $2S$-$4S$,$4D$ two-photon transition frequencies, we have determined the $1S$ Lamb shift to an accuracy of 7 parts in 10^6 and 1 part in 10^5 for hydrogen and deuterium, respectively. The precision exceeds the accuracy of earlier measurements and also that of radio frequency measurements of the $2S$ Lamb shift. While ours as well as earlier measurements of the hydrogen $1S$ and $2S$ Lamb shifts are in agreement with quantum electrodynamic theory, the agreement between theory and experiment for the $2S$ Lamb shift in He^+ is presently poor. An alternative interpretation of our hydrogen $1S$ Lamb shift result assumes the "completeness" of quan-

TABLE VII. Comparison of the theoretical values with the experimental results for the atomic difference frequencies $(E_{4S,4D}-E_{2S})-\frac{1}{4}(E_{2S}-E_{1S})$ (hyperfine centroids), and determination of the $1S$ Lamb shift (all data).

	Hydrogen		Deuterium	
	$2S_{1/2}$-$4S_{1/2}$ (MHz)	$2S_{1/2}$-$4D_{5/2}$ (MHz)	$2S_{1/2}$-$4S_{1/2}$ (MHz)	$2S_{1/2}$-$4D_{5/2}$ (MHz)
$(E_{4S,4D}-E_{2S})-\frac{1}{4}(E_{2S}-E_{1S})$				
Theory	4797.329(5)	6490.128(5)	4801.692(5)	6494.816(5)
Experiment	4797.338(10)	6490.144(24)	4801.693(20)	6494.841(41)
Dirac and reduced mass corr.	−3928.707(0)	−5752.644(1)	−3931.867(0)	−5757.301(1)
$\frac{1}{4}L_{1S}-\frac{5}{4}L_{2S}+L_{4S,4D}$	868.631(10)	737.450(24)	869.826(20)	738.540(41)
$\frac{5}{4}(L_{2S_{1/2}}-L_{2P_{1/2}})$ [a]	1322.306(11)	1322.306(11)		
Theoretical Lamb shifts [b]	−147.702(2)	−16.581(2)	1176.122(8)	1307.432(8)
$\frac{1}{4}L_{1S}$ Lamb shift	2043.217(15)	2043.225(26)	2045.948(22)	2045.972(42)

[a]Exp. $2S_{1/2}$-$2P_{1/2}$ Lamb shift [2].
[b]For hydrogen: $\frac{5}{4}L_{2P_{1/2}}-L_{4S,4D_{5/2}}$; for deuterium: $\frac{5}{4}L_{2S}-L_{4S,4D_{5/2}}$.

TABLE VIII. Error contributions to the experimental $1S$ Lamb shift in hydrogen and deuterium (all data).

	Hydrogen (kHz)	Deuterium (kHz)
Statistical error	30	43
Line shape	15	18
Zeeman shift	9[a]	63[a]
dc Stark effect	4	4
Reference cavity drift	11	11
Second-order Doppler shift:		
$1S$-$2S$	3	2
$2S$-$4S$,$4D$	16	10
Expt. $2S_{1/2}$-$2P_{1/2}$ Lamb shift [b]	45	
Theoretical Lamb shifts	8[c]	30[d]
rms sum	60	78

[a]Third data set only.
[b]Reference [2].
[c]$L_{2P_{1/2}}$, $L_{4S_{1/2}}$, and $L_{4D_{5/2}}$.
[d]$L_{2S_{1/2}}$, $L_{4S_{1/2}}$, and $L_{4D_{5/2}}$.

tum electrodynamic theory and yields a determination of the proton charge radius which is found to be in agreement with the value given by Simon *et al.* [10] based on electron scattering experiments. From a comparison of our measured deuterium and hydrogen Lamb shifts we find a value for the nuclear matter radius of the deuteron.

For future, even more precise Lamb shift measurements it seems reasonable to compare the experimental value of the difference frequency of $2S$-$4S$ and a quarter of $1S$-$2S$ directly with the corresponding theoretical value as a test of QED, since our present determination of the ground state Lamb shift is largely limited by the uncertainty in the $2S$ Lamb shift. This difference frequency determines a compound "hyper-Lamb-shift" $\frac{1}{4}L_{1S} - \frac{5}{4}L_{2S} + L_{4S}$. Karshenboim has suggested alternatively to make use of the fact that the small deviation in the $1/n^3$ scaling law of the Lamb shifts is comparatively well known [60] which allows a determination of both the $1S$ and $2S$ Lamb shifts from $\frac{1}{4}L_{1S} - \frac{5}{4}L_{2S} + L_{4S}$ [9].

Substantial further improvements in precision should be possible by using the optically excited slow metastable beam of the $1S$-$2S$ spectrometer for excitation into the $4S$ state, which is currently being investigated in Garching. At the expense of the simplicity of the frequency comparison with $1S$-$2S$, and with higher sensitivity to stray electric fields, alternatively transitions from $2S$ into a higher Rydberg nS or nD state ($n>4$) with a smaller natural linewidth can be excited. Detection of the nS-$2P$ fluorescence similar to the present experimental setup is especially well suited for spectroscopy on an optically excited metastable hydrogen beam, since there is less stray light at the detection wavelength. In the current experimental setup the obtained signal to noise ratio of the $2S$-$4S$ spectrometer is limited by stray light from the electron gun filament.

An alternative possibility for a comparison of hydrogen transition frequencies is to choose the $1S$-$3S$ and $2S$-$6S$ two-proton transitions. Such an experiment is currently being performed in Paris. The advantage of the $2S$-$6S$ transition compared to $2S$-$4S$ is a smaller natural linewidth (298 kHz)

TABLE IX. Some recent laser spectroscopic measurements of the $1S$ Lamb shift in hydrogen and deuterium and comparison with theory.

	$1S$ Lamb shift (MHz)	Excitation of $1S$-$2S$	Frequency comparison
	Hydrogen		
Hänsch *et al.* [4]	8600 (800)	pulsed	$2S$-$4P$
Lee *et al.* [54]	8220 (100)	pulsed	$2S$-$4P$
Wieman and Hänsch [55]	8175 (30)	pulsed	$2S$-$4P$
Beausoleil *et al.* [6]	8173.3 (1.7)	cw	Tellur. std.
Boshier *et al.* [7]	8172.6 (0.7)	cw	Tellur. std.
Weitz *et al.* [11]	8172.82 (0.11)	cw	$2S$-$4S$,$4D$
Garching $1S$-$2S$ and Paris $2S$-$8S$,$8D$ [14]	8172.815 (0.070)	cw	He-Ne std.
This work	8172.874 (0.060)	cw	$2S$-$4S$,$4D$
Theory:			
old	8173.097 (0.040)		
with two-loop corr [8,9].	8172.802(0.040)		
	Deuterium		
Hänsch *et al.* [4]	8300 (830)	pulsed	$2S$-$4P$
Lee *et al.* [54]	8260 (110)	pulsed	$2S$-$4P$
Wieman and Hänsch [55]	8189 (30)	pulsed	$2S$-$4P$
Boshier *et al.* [7]	8183.7 (0.6)	cw	Tellur. std.
This work	8183.807 (0.078)	cw	$2S$-$4S$, $4D$
Theory:			
old	8184.080 (0.047)		
with two-loop corr. [8,9].	8183.785(0.047)		

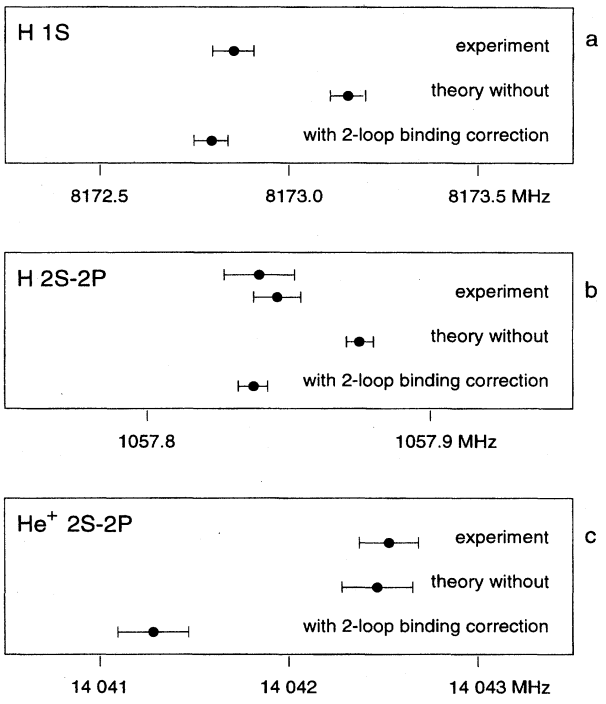

FIG. 12. Comparison of experimental hydrogen $1S$ (this work) and $2S$-$2P$ (Refs. [2] and [3]), and He^+ $2S$-$2P$ (Ref. [15]) Lamb shift with the theoretical prediction including and without recently calculated two-loop binding corrections [8,9]. For the theoretical hydrogen Lamb shifts we assume a proton charge radius as given in Ref. [10], assuming an older measurement for the proton charge radius [52] the theoretical values for hydrogen decrease by 149 kHz/n^3.

and a larger transition probability [43]. However, the difficulty is the observation of the $1S$-$3S$ two-photon transition with an excitation wavelength of 205 nm. A first signal has recently been observed on this transition, which should lead to an improvement of the measurement of the $1S$ Lamb shift.

More precise measurements of the proton charge radius would then permit a test of QED with still higher precision. Laser spectroscopy of muonic hydrogen should provide a more accurate nuclear charge radius in future [56]. In this exotic atom, due to its small Bohr radius ($m_{\mu on} \approx 207 m_e$), nuclear size effects have a considerably larger influence on the energy levels. A precise measurement of the $2S$-$2P$ splitting in muonic hydrogen should allow a determination of the proton charge radius to an uncertainty of 1 part in 10^3.

An alternative method for a precise Lamb shift measurement in hydrogen involves an excitation of the $2S$-$4S$ transition using a 486-nm laser beam resonant with $2S$-$4P$ and a radio frequency resonant with $4P$-$4S$ (or $2S$-$2P$ and $2P$-$4S$, respectively). Spontaneous emission from the intermediate short-lived P state can be avoided when the transfer is done using adiabatic passage, based on a slow change of the Rabi frequencies of the two fields, via a dark superposition state of $2S$ and $4S$. A high frequency resolution and a Doppler-free resonance can be achieved when an atomic interferometer method with four adiabatic pulses is used. This method has previously been demonstrated in a Raman level scheme [61]. It has been shown that using this method with resonant light, no ac Stark shift in a pure three-level system occurs even when the transfer is not completely adiabatic [62]. In the present hydrogen experiment the systematic uncertainties are dominated by the amount to which the ac Stark shift of the exciting laser field can be corrected for. We have performed a preliminary analysis of the effect of the additional levels present for an adiabatic transfer between the hydrogen $2S$ and $4S$ levels, suggesting a transfer from $2S(F=1), m_F=1$ to $4S(F=1), m_F=1$ via $4P(F=2), m_F=2$.

ACKNOWLEDGMENTS

This work has been supported in part by the Deutsche Forschungsgemeinschaft and within the frame of an ECC SCIENCE program cooperation, Contract No. SC1*-CT92-0816.

[1] *The Hydrogen Atom*, edited by G. F. Bassani, M. Inguscio, and T. W. Hänsch (Springer, Berlin, 1989).

[2] S. R. Lundeen and F. M. Pipkin, Phys. Rev. Lett. **46**, 232 (1981).

[3] E. W. Hagley and F. M. Pipkin, Phys. Rev. Lett. **72**, 1172 (1994).

[4] T. W. Hänsch, S. A. Lee, R. Wallenstein, and C. Wieman, Phys. Rev. Lett. **34**, 307 (1975).

[5] F. Schmidt-Kaler, D. Leibfried, S. Seel, C. Zimmermann, W. König, M. Weitz, and T. W. Hänsch, Phys. Rev. A **51**, 2789 (1995).

[6] R. G. Beausoleil, D. H. McIntyre, C. J. Foot, E. A. Hildum, B. Couillaud, and T. W. Hänsch, Phys. Rev. A **35**, 4878 (1987).

[7] M. G. Boshier, P. E. G. Baird, C. J. Foot, E. A. Hinds, M. D. Plimmer, D. N. Stacey, J. B. Swan, D. A. Tate, D. M. Warrington, and G. K. Woodgate, Phys. Rev. A **40**, 6169 (1989).

[8] K. Pachucki, Phys. Rev. Lett. **72**, 3154 (1994).

[9] K. Pachucki, D. Leibfried, M. Weitz, A. Huber, W. König, and T. W. Hänsch (unpublished).

[10] G. G. Simon, Ch. Schmitt, F. Borkowski, and V. H. Walther, Nucl. Phys. A **333**, 381 (1980).

[11] M. Weitz, F. Schmidt-Kaler, and T. W. Hänsch, Phys. Rev. Lett. **68**, 1120 (1992).

[12] M. Weitz, A. Huber, F. Schmidt-Kaler, D. Leibfried, and T. W. Hänsch, Phys. Rev. Lett. **72**, 328 (1994).

[13] T. Andreae, W. König, R. Wynands, D. Leibfried, F. Schmidt-Kaler, C. Zimmermann, D. Meschede, and T. W. Hänsch, Phys. Rev. Lett. **69**, 1923 (1992).

[14] F. Nez, M. D. Plimmer, S. Bourzeix, L. Julien, F. Biraben, R. Felder, Y. Millerioux, and P. de Natale, Europhys. Lett. **24**, 635 (1993).

[15] A. van Wijngaarden, J Kwela, and G. W. F. Drake, Phys. Rev. A **43**, 3325 (1991).

[16] F. Schmidt-Kaler, D. Leibfried, M. Weitz, and T. W. Hänsch,

Phys. Rev. Lett. **70**, 2261 (1993).
[17] W. R. Johnson and G. Soff, At. Data Nucl. Data Tables **33**, 405 (1985).
[18] G. W. Erickson, J. Phys. Chem. Ref. Data **6**, 831 (1977).
[19] J. R. Sapirstein and D. R. Yennie, in *Quantum Electrodynamics*, edited by T. Kinoshita (World Scientific, Singapore, 1990).
[20] K. Pachucki and H. Grotch, Phys. Rev. A **51**, 1854 (1995); K. Pachucki, Phys. Rev. A **52**, 1079 (1995).
[21] K. Pachucki, D. Leibfried, and T. W. Hänsch, Phys. Rev. A **48**, R1 (1993).
[22] K. Pachucki, M. Weitz, and T. W. Hänsch, Phys. Rev. A **49**, 2255 (1993).
[23] S. Klarsfeld, J. Martorell, J. A. Oteo, M. Nishimura, and D. W. L. Sprung, Nucl. Phys. A **456**, 373 (1986).
[24] K. Pachucki and S. G. Karshenboim, J. Phys. B **28**, L221 (1995).
[25] E. R. Cohen and B. N. Taylor, Rev. Mod. Phys. **59**, 1121 (1987).
[26] R. S. van Dyck, Jr. *et al.* (unpublished).
[27] This value was computed by M. Bradley from nuclear masses given in G. Audi and A. H. Wapstra, Nucl. Phys. A **565**, 1 (1993).
[28] C. Zimmermann, R. Kallenbach, and T. W. Hänsch, Phys. Rev. Lett. **65**, 571 (1990).
[29] R. W. P. Drever, J. L. Hall, F. V. Kowalski, J. Hough, G. M. Ford, A. J. Munley, and H. Ward, Appl. Phys. B **31**, 97 (1983).
[30] W. Vassen, C. Zimmermann, R. Kallenbach, and T. W. Hänsch, Opt. Commun. **75**, 435 (1990).
[31] M. Weitz, F. Schmidt-Kaler, and T. W. Hänsch, in *Solid State Lasers*, edited by M. Inguscio and R. Wallenstein (Plenum, New York, 1993).
[32] J. Hall (private communication).
[33] F. Biraben, J. C. Garreau, L. Julien, and M. Allegrini, Rev. Sci. Instrum. **61**, 1468 (1990).
[34] J. T. M. Walraven and I. F. Silvera, Rev. Sci. Instrum. **53**, 1167 (1982).
[35] W. H. Wing, Appl. Opt. **18**, 2346 (1979).
[36] H. A. Bethe and E. E. Salpeter, *Quantum Mechanics of One- and Two-Electron Atoms* (Plenum, New York, 1977).
[37] T. W. Welford and R. Winston, *High Collection Nonimaging Optics* (Academic, San Diego, 1989).
[38] R. T. Robiscoe and T. W. Shyn, Phys. Rev. Lett. **24**, 559 (1970).
[39] T. W. Hänsch and B. Couillaud, Opt. Commun. **35**, 441 (1980).
[40] W. Winkler, K. Danzmann, A. Rüdiger, and R. Schilling, Phys. Rev. A **44**, 7022 (1991).
[41] M. Weitz, Ph.D. thesis, LMU-München, 1992 (unpublished).
[42] L. S. Vasilenko, V. P. Chebotayev, and A. V. Shishaev, Pis'ma Zh. Eksp. Teor. Fiz. **12**, 161 (1970) [JETP Lett. **12**, 113 (1970)]; B. Cagnac, G. Grynberg, and F. Biraben, J. Phys. (Paris) **34**, 845 (1973).
[43] J. C. Garreau, M. Allegrini, L. Julien, and F. Biraben, J. Phys. France **51**, 2263 (1990); **51**, 2275 (1990); **51**, 2293 (1990).
[44] F. Bassani, J. J. Forney, and A. Quattropani, Phys. Rev. Lett. **39**, 1070 (1977).
[45] R. G. Beausoleil and T. W. Hänsch, Phys. Rev. A **33**, 1661 (1986).
[46] J. M. Harriman, Phys. Rev. **101**, 594 (1956).
[47] H. Kogelnik and T. Li, Appl. Opt. **5**, 1550 (1966).
[48] P. R. Bevington, *Data Reduction and Error Analysis for the Physical Sciences* (McGraw-Hill, New York, 1969).
[49] For hydrogen $1S$: H. Hellwig, R. F. C. Vessot, M. W. Levine, P. W. Zizewitz, D. W. Allan, and D. J. Glaze, IEEE Trans. Instrum. Meas. **IM-19**, 200 (1970); L. Essen, R. W. Donaldson, M. J. Bangham, and E. G. Hope, Nature **229**, 110 (1971). For deuterium $1S$: D. J. Wineland and N. F. Ramsey, Phys. Rev. A **5**, 821 (1972); N. F. Ramsey, in *Quantum Electrodynamics*, edited by T. Kinoshita (World Scientific, Singapore, 1990). For hydrogen $2S$: J. W. Heberle, H. A. Reich, and P. Kusch, Phys. Rev. **101**, 612 (1956). For deuterium $2S$: H. A. Reich, J. W. Heberle, and P. Kusch, Phys. Rev. **104**, 1585 (1956).
[50] E. A. Hinds, in *The Hydrogen Atom* (Ref. [1]).
[51] G. Breit, Phys. Rev. **35**, 1447 (1930).
[52] L. N. Hand, D. G. Miller, and R. Wilson, Rev. Mod. Phys. **35**, 335 (1963).
[53] The small difference of these results to those given in Ref. [12] are mainly due to the new theoretical contributions to the Lamb shifts of the states $4S$ and $2P$ for hydrogen and $4S$ and $2S$ for deuterium.
[54] S. A. Lee, R. Wallenstein, and T. W. Hänsch, Phys. Rev. Lett. **35**, 1262 (1975).
[55] C. Wieman and T. W. Hänsch, Phys. Rev. A **22**, 192 (1980).
[56] D. Taqqu (private communication).
[57] D. W. L. Sprung and H. Wu, Acta Physica Pol. B **24**, 503 (1993).
[58] J. L. Friar, G. L. Payne, V. G. J. Stoks, and J. J. de Swart, Phys. Lett. B **311**, 4 (1993).
[59] From the hydrogen $1S$-$2S$ transition frequency we determine the $2P$-$4S$,$4D$ hydrogen absolute frequency using our measured hydrogen $(E_{4S,4D}$-$E_{2S})$-$\frac{1}{4}(E_{2S}$-$E_{1S})$ difference frequency and the $2S$-$2P$ splitting of Ref. [2], from which the Rydberg constant is derived using theoretical values for the well-known $2P$ and $4S$,$4D$ Lamb shifts. We also determine the deuterium $2S$-$4S$,$4D$ difference frequency from the hydrogen $1S$-$2S$ frequency using the hydrogen deuterium isotope shift of $1S$-$2S$ [16] and our measured deuterium $(E_{4S,4D}$-$E_{2S})$-$\frac{1}{4}(E_{2S}$-$E_{1S})$ difference frequency, from which we derive a second value for the Rydberg constant using theoretical values for the deuterium $2S$ and $4S$ Lamb shifts. The quoted result for the Rydberg constant is a weighted average of both values.
[60] S. G. Karshenboim, Zh. Eksp. Teor. Fiz. **106**, 414 (1994) [JETP **79**, 230 (1994)].
[61] M. Weitz, B. C. Young, and S. Chu, Phys. Rev. Lett. **73**, 2563 (1994).
[62] M. Weitz, B. C. Young, and S. Chu, Phys. Rev. A **50**, 2438 (1994).